

Experimental and numerical study of hybrid (CFRP-GFRP) composite laminates containing circular cut-outs under shear loading

Mahdi Damghani ^{a,*}, Rakib Ali Pir ^a, Adrian Murphy ^b, Mohammad Fotouhi ^c

^a Department of Engineering, Design and Mathematics (EDM), University of the West of England (UWE), Bristol, BS16 1QY, UK

^b School of Mechanical and Aerospace Engineering, Queen's University Belfast (QUB), Belfast, BT9 5AG, UK

^c James Watt School of Engineering, University of Glasgow, Glasgow, G12 8QQ, UK

Abstract

Previous works have established the response and failure behaviour of hybrid (CFRP-GFRP) laminates when subjected to a wide range of destabilising loads. However, to date no works have focused on plates with cut-outs under shear loading and quantified the influence of selective laminate shapes and hybridisation on their post-buckling response. Herein, the plate collapse behaviour of a novel X-braced hybrid (CFRP-GFRP) twill woven laminate containing a large circular cut-out (diameter to width ratio of 0.35), subjected to in-plane shear loading is investigated. The study includes a hybrid and a baseline pure CFRP design and employs both experimental and numerical analysis. The experimental results illustrate that despite having less CFRP material, a hybrid laminate design with shaped CFRP plies exhibits greater failure load (+9%), and a greater failure load to buckling load ratio (1.26 compared to 1.12). However, this comes at the cost of a marginally lower initial plate buckling load (-3%). Additionally, the combined experimental and numerical analysis reveals the detailed failure mechanism of both the pure CFRP and hybrid laminates, revealing similar behaviour but that the hybrid design endures significantly more widespread shear damage of the matrix.

Keywords: shear buckling, laminated composites, hybrid composites, post-buckling behaviour, nonlinear behaviour, cut-out

* Corresponding author. Tel.: +4411732 87369
Email address: Mahdi.Damghani@uwe.ac.uk

1 Introduction

Since the 1980s, there has been continuous growth in the use of Carbon Fibre Reinforced Polymer (CFRP) and Glass Fibre Reinforced Polymer (GFRP) laminated composites for the manufacture of aircraft structures. The key drivers for such sustained growth are lighter weight, higher operating temperatures, greater stiffness, higher reliability, better design flexibility and increased affordability of the materials. CFRP and GFRP also offer special properties, like good radio-frequency compatibility of fiberglass radomes [3]. Although traditional materials such as aluminium alloys provide high strength and high stiffness at low weight, they are susceptible to corrosion and fatigue. Airframe corrosion and fatigue problems tend to arise in operations (post design) and are expensive to tackle for aircraft Original Equipment Manufacturers (OEM). As such CFRP and GFRP have been developed and applied widely on larger aircraft [4] to meet the requirements of enhanced structural performance and reduced maintenance costs [5].

The use of CFRP and GFRP in commercial aircraft was first limited to secondary structures such as inspection panels, spoilers, or air brakes. This reduced risk and led to improved understanding in-operations, enabling the collection of data from test and fleet experience. Enhancements in manufacturing technology, the development of innovative material systems and a better understanding of their mechanical behaviour have now led to the use of composites for primary aircraft structures (first in empennage structures, before use in wing skin, fuselage structures, etc). Primary aircraft structures are typically thin-walled shell structures, and generally an assemblage of plate elements which are expected to carry a variety of loads resulting from aerodynamic pressure, inertial forces stemming from various manoeuvres, etc. [6].

Although composite materials have been extensively employed in aircraft structural design, their full potential has yet to be realised. That of tailoring the shape of CFRP/GFRP plies to the loading direction on a local plate level has not been widely studied. **Instead, the research has focused on variable angle tow composites [7] neglecting the benefits of ply shaping of conventional composites particularly with the advent of advanced topology and sizing optimisation techniques.** Another flexibility is to utilise plate residual strength after buckling, post-buckling, which is often ignored in current design and sizing methodologies given that the post-buckling behaviour of

composite panels is stable. This is because the post-buckling and collapse behaviour of thin laminated composite structures in operations is not well understood. It should be noted that for aerostructures, the degree of post-buckling allowed depends on the type of structure, and the aerodynamic constraints. For example, buckling of the upper wing cover would not be appropriate during typical operations as this would significantly impact the flow of air over the wing and the aerodynamic performance of the aircraft. Thus, wing and empennage skin panels are mostly held buckling resistant. On the other hand, fuselage panels, ribs and spars within the wing box are permitted to have post-buckling designs [8].

In preceding work, the authors proposed the use of X-shaped CFRP plies within hybrid CFRP-GFRP composite plates [1], and examined their performance under shear loading. The experimental and simulation work demonstrated improved ratios between failure and buckling loads, and substantially higher strain to failure behaviour, compared to non-hybrid conventional composite plate designs. Such plate elements could have extensive use as wing spar webs where shear is the dominant loading and plate post-buckling behaviour is allowed. However, such structures typically exhibit cut-outs and holes to provide access to electrical, hydraulic and fuel lines, as well as inspection windows [9]. The presence of cut-outs will influence plate design structural stability and strength. Thus, it is important to understand the buckling, post-buckling response, damage, and failure characteristics of hybrid CFRP-GFRP plates containing cut-outs.

The objective of this paper is thus to determine and compare the shear buckling and post-buckling behaviour of a conventional laminate plate containing a circular cut-out against a CFRP-GFRP plate with selective ply shapes. The following section presents a focused review of recent literature, in the last five years, considering composite structures, hybrid CFRP-GFRP laminates, buckling, post-buckling, shear loading and cut-outs. This is followed by a detailed description of the experimental program undertaken comparing conventional and hybrid laminate designs. This is followed with simulation **studies**, based on the experimental specimen designs, to study the detail damage mechanisms and how these differ between the conventional and hybrid laminate. The paper is then concluded with a discussion and summary of the key findings.

2 Literature review

The problems of stability and load-carrying capacity of thin-walled composite structures have been studied for over four decades [10], [11], particularly in aerospace and automotive applications. Although much of the past works were focused on the development of analytical solutions, more recent work typically employs Finite Element Analysis (FEA) to examine novel loading events, materials, or structural designs. This is thanks to versatile commercial simulation tools and lower cost High Performance Computing (HPC). Due to the abundance of research in this field the review focuses on the most relevant research carried out in the last five years.

Kolanu et al. [12] investigated the buckling and post-buckling behaviour of both pristine and defect embedded (de-bonded) single blade stiffened CFRP panels under uniaxial compression loading. They used a progressive damage model and FEA to model the initiation and evolution of both intra-laminar and inter-laminar damage. They reported differences of less than 3% in collapse load values and less than 4% in end-shortening displacements between experimental and numerical procedures. Castriota et al. [13] studied the buckling behaviour of a CFRP panel with multiple reinforcements with and without simulated **damage**. They used experimental procedures and validated a linear FEA buckling analysis. They concluded that the presence of the damage did not influence the buckling behaviour. However, they did not consider progressive damage analysis and post-buckling response. The experimental study of low velocity impacted CFRP stiffened panels under axial and multiaxial loading conditions and their buckling and load-bearing behaviour have been studied by Fernandez et al. [14]. They considered two panel configurations - in the first configuration, the stiffeners were stitched to the skin. In the second configuration, the panels were unstitched. The tests showed that undamaged, stitched specimens have a lower failure load compared to the unstitched specimens. However, when damaged the stitched panels had a higher failure load. Feng et al. [15] carried out experimental and numerical studies of the buckling and post-buckling behaviour of stiffened composite panels under axial compressive loading. The highlight of their work was that the average failure load was 2.43 times larger than the average buckling load. Their buckling and failure load predictions, using FEA and progressive damage modelling had 3.8% and 4.4% error, respectively, compared to the experimental results.

Generally, the existence of cut-outs in structures alters stress and strain distribution and may lead to reduced load bearing capacity. Significantly, the stress/strain concentrations are reported to be considerably higher for composite structures than their metallic counterparts [16], [17]. Unlike metallic structures, composite structures do not exhibit yielding and plastic deformations around cut-outs, but the brittle nature of CFRP material makes them vulnerable to sudden brittle failure. Zhang et al. [18] showed that the existence of **two separate cut-outs** in a CFRP I-beam created a complex strain distribution under buckling and post-buckling response, compared to a single cut-out. Celebi et al. [19] carried out studies on the effect of cut-outs with varying circumferential locations and sizes for both constant stiffness and variable-stiffness cylindrical shells with steered fibres under pure bending. It was demonstrated that the existence of cut-outs and elevated stresses around them could trigger local buckling. They also observed that the location and size of cut-outs within the cylindrical shell structure had a significant impact on the buckling and ultimate failure load. Li et al. [20] showed the negative effect of cut-outs on buckling and post-buckling response. They examined variable stiffness designs to improve the post-buckling performance but found that in most cases both the pre- and post-buckling stiffness were reduced with increasing cut-out opening size.

Hybridisation has been used by many researchers to improve structural performance under various loading conditions. Amongst the demonstrated structural performance enhancements are better residual strength after impact [21], notch sensitivity reduction [22], improving buckling [23] and post-buckling responses [1], enhancing fatigue performance [24]. For example, Taraghi et al. [25] used CFRP reinforcement on steel conical shells (hybrid CFRP-steel) under uniform pressure loading to improve the buckling response. In a later work [23], they used FEA to design and study the effect of ply orientation and shape of CFRP strip reinforcement on overall buckling and post-buckling response of the structure and validated their work with experiments. Maali et al. [26] used CFRP wrapping of cylindrical steel shells to improve buckling and post-buckling response under hydrostatic pressure. Vummadisetti et al. [27] studied buckling and post-buckling performance of functionally graded hybrid laminates and sandwich hybrid laminates with and without various size cut-outs under uni-axial compressive loading. The overarching conclusion was that functionally graded hybrid laminates had better buckling and failure load compared to

other hybrid laminates but never managed to match the buckling load of pure CFRP plates. This was due to the high stiffness of CFRP plies compared to other material types confirming the findings of the work by the authors [1]. Moreover, they showed that plates with smaller size cut-outs had higher critical buckling and first failure loads. Hybridisation, has also been used to obtain a more ductile (pseudo-ductile) behaviour to match the stress-strain curve of conventional metallic materials [28]. The main objective of such an approach is to minimise the abrupt catastrophic failure of CFRP structures and hence use smaller margins of safety. For a literature review of using CFRP-GFRP hybridisation for pseudo-ductile behaviour the reader is referred to [29].

Based on the above, it is evident from the literature that CFRP composite laminates containing cut-outs have complex and elevated stresses/strains leading to reductions in both buckling and post-buckling performance. Given the brittleness of CFRP materials and in the presence of the cut-out, this could lead to an abrupt and catastrophic failure. On the other hand, laminated composites have considerable strength after initial buckling, but this is not always used in design. Laminate hybridisation has been proposed to address this weakness [1], where the CFRP-GFRP hybridisation has been shown to enhance structural performance under destabilising shear loading, and to reduce brittleness, evidenced by obtaining high strains at failure. However, the buckling and post-buckling behaviour of such a design in the presence of a large cut-out has not been investigated.

Despite the developed knowledge on the buckling and post-buckling behaviour of composite laminates, there is very limited work on the damage mechanisms of hybrid CFRP-GFRP woven fabric composite laminates containing cut-outs. In particular, for in-plane shear loading, there are very few works which fully characterise post-buckling damage behaviour. Hence, this paper presents a combined experimental and numerical simulation study. A conventional laminate and a novel CFRP-GFRP laminate with selective laminate shapes will be tested. The design, proposed in [1], has already demonstrated improved behaviour under shear loading. Thus, buckling, post-buckling and collapse behaviour will be experimentally captured and modelled using FEA with progressive damage modelling (to further examine the post-buckling damage behaviours). This will identify whether the condition of equivalent or equal initial buckling can be achieved while also achieving an increase in post-buckling reserve, and how damage in the post-buckling regime influences this performance.

Based on the literature review, the remaining paper content is arranged as follows: Section 3 introduces the design of the novel CFRP-GFRP laminate with selective laminate shapes, and an appropriate baseline laminate design. Section 4 presents the Finite Element (FE) modelling approach which will be used to understand the differences in post-buckling damage mechanisms between the conventional and novel laminate designs. The experimental procedure for laminate post-buckling testing is presented in section 5. Finally, results and discussions are given in section 6 and conclusions are made in section 7.

3 Laminate design

Herein, two laminate types will be studied. In type 1, the entire laminate is made of woven twill CFRP with a quasi-isotropic stacking sequence of $[\pm 45/\pm 45/0/0]_S$. This is the baseline laminate in which all CFRP plies are square in shape and have dimensions of $200\text{ mm} \times 200\text{ mm}$. Type 2 laminate is a hybrid laminate in which woven twill GFRP plies are placed at the outer and inner mould surfaces. In this hybrid laminate design, both the GFRP and CFRP plies of $0/90^\circ$ angle have a square shape with size $200\text{ mm} \times 200\text{ mm}$. In the type 2 laminates, the CFRP plies are angled at $\pm 45^\circ$ and have an X shape, with width of $W = 60\text{ mm}$, as shown in Figure 2. In the preceding work [1], a parametric study (without cut-out) was used to define the width of the X shape to obtain equivalent buckling load and match the type 1 design. The ply shaping was intended to partly reduce the mass resulting from the use of the addition of the GFRP plies. The stacking sequence for the type 2 laminate is $[\pm 45G/\pm 45_X/\pm 45_X/0/0]_S$ where G and subscript X represent GFRP and X-shape CFRP plies, respectively.

In this study, each specimen design will have a circular cut-out of diameter $D = 64\text{ mm}$. The cut-out dimension has been selected to represent the ratio of geometry found in civil aircraft structures. For example, a typical track cut-out in a wing spar will have an approximate $D/L = 0.35$ ratio (see Figure 1). Where D and L are the diameter of the cut-out and width of the spar plate between reinforcing stiffeners, respectively. It should be noted that using the previously mentioned design configuration led to the type 1 and type 2 designs being 99.25 grams and 125 grams, respectively.

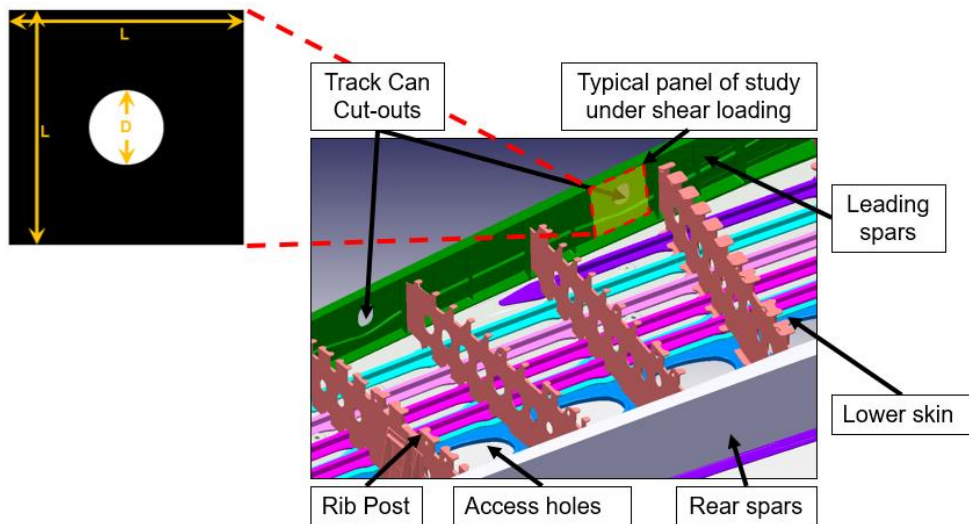


Figure 1: A digital mock-up of lower wing of a civil aircraft (upper skin removed)

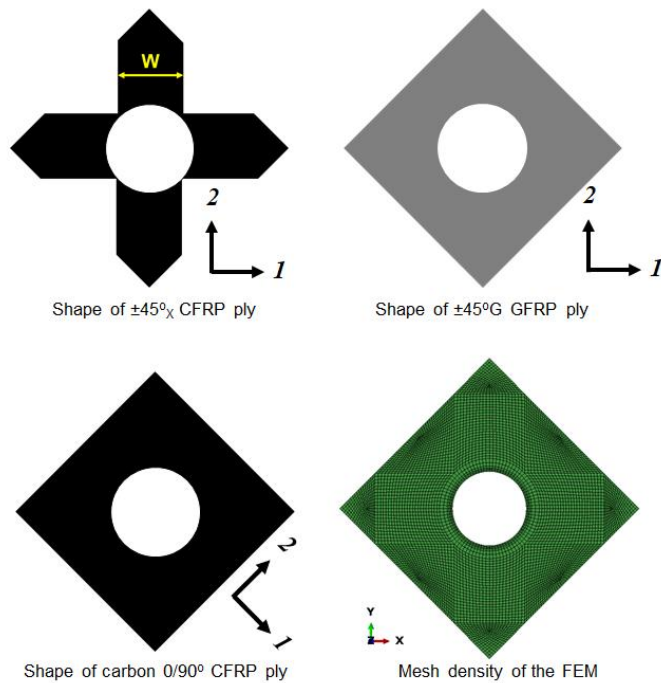


Figure 2: Ply shapes and mesh density of the laminates (X and G represent X-shaped CFRP ply and GFRP ply, respectively).

4 Finite Element Analysis (FEA)

4.1 Finite Element Model (FEM)

The commercial finite element software ABAQUS [30] is used for the modelling studies. Quadrilateral (with 4 nodes), general-purpose shell, reduced integration with hourglass control, finite membrane strain elements (S4R) are used to model the laminate. Three integration points through the thickness were chosen for each ply. This leads to a total of 24 and 30 integration points through the thickness for type 1 and type 2 laminates, respectively. Measured cured ply thickness data, Table 1, is

used within the FE model for both the CFRP and GFRP plies. As shown in Figure 3, the purple edges were constrained to a reference point (purple reference point) at the bottom of the laminate using kinematic coupling for all Degrees Of Freedoms (DOF) except for the displacement DOF perpendicular to the edge. It is worth noting that kinematic coupling constrains the motion of the coupling nodes to the rigid body motion of the reference node. The purple reference point was fully clamped, i.e. all displacement and rotational DOFs were fully constrained. Conversely, the green edges were kinematically constrained to a reference point (green reference point) at the topmost location of the laminate for all DOFs except for displacement DOF perpendicular to the edge. For the green reference point, all DOFs except for displacement in y direction were constrained. Red edges were not included in the kinematic constraint to represent the free edges of the experimental set-up. Then, a prescribed displacement of 4.5 mm was given for the displacement in the y direction. Defining interactions in this manner would ensure that all edges of the laminate act as a rigid edge similar to that of the experimental test set-up [1], [9].

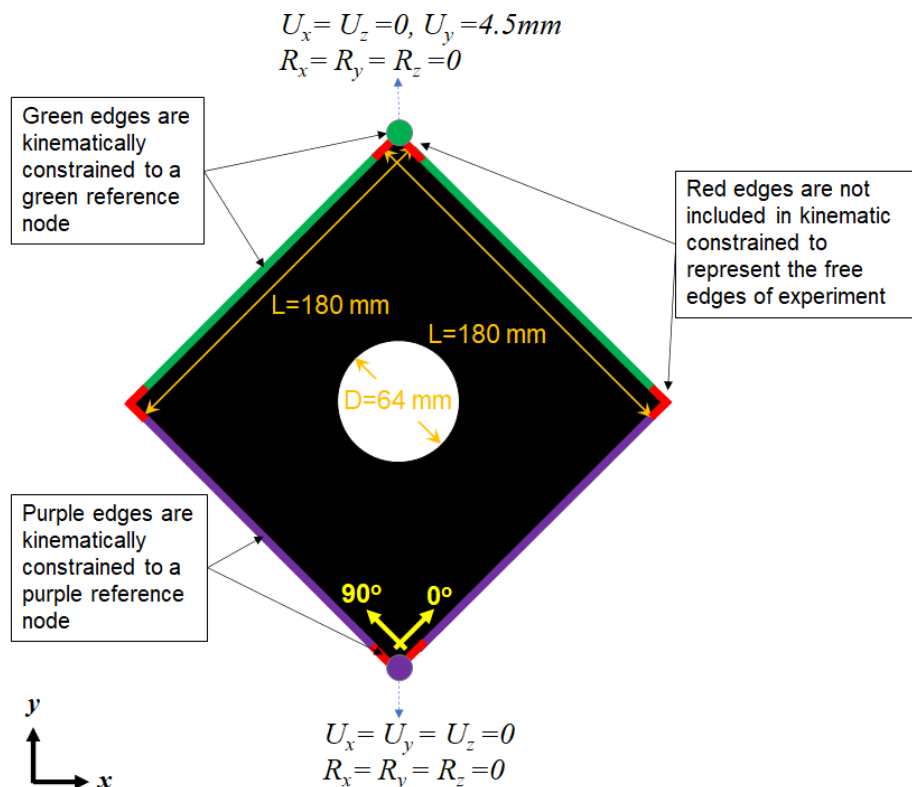


Figure 3: Loading (imposed displacement), boundary conditions

4.2 Material model

The bi-directional nature of the twill materials used in the study means that common conventional material failure criteria such as Hashin, which were originally developed for uni-directional polymeric composites, are not appropriate [1]. Thus, a constitutive material model from the literature, developed for fabric reinforced composites, is used. The fabric ply failure model is implemented within a built-in VUMAT user subroutine in ABAQUS/Explicit.

In the material model, the fabric-reinforced ply is represented as a homogenous orthotropic elastic material. The material model considers progressive stiffness degradation stemming from fibre damage and matrix cracking and plastic deformation under loading. Thus, it is assumed that there are two main failure mechanisms: fibre dominated failure in tension or compression in the two fibre directions; and matrix dominated failure in in-plane shear [31], [32]. The mechanisms of failure are briefly discussed hereafter and further detailed in [33].

4.2.1 Elastic stress-strain relationship

Orthotropic damaged elasticity is used to define the material elastic stress-strain relations. The relation is formulated in a local coordinate system aligned with the fibre direction;

$$\begin{bmatrix} \varepsilon_{11} \\ \varepsilon_{22} \\ \varepsilon_{12}^{el} \end{bmatrix} = \begin{bmatrix} \frac{1}{(1-d_1)E_1} & \frac{-\nu_{12}}{E_1} & 0 \\ \frac{-\nu_{21}}{E_2} & \frac{1}{(1-d_2)E_2} & 0 \\ 0 & 0 & \frac{1}{(1-d_{12})2G_{12}} \end{bmatrix} \begin{bmatrix} \sigma_{11} \\ \sigma_{22} \\ \sigma_{12} \end{bmatrix} \quad (1)$$

E_1 and E_2 are Young's moduli in the principal orthotropic directions, G_{12} is the in-plane shear modulus, and ν_{12} is the principal Poisson's ratio. d_1 ($0 \leq d_1 \leq 1$) and d_2 ($0 \leq d_2 \leq 1$) are scalar damage variables which are associated to fibre micro-cracks and fracture along the ply 1 and 2 directions, respectively; and d_{12} ($0 \leq d_{12} \leq 1$), which is associated to matrix micro-cracking as a result of shear deformation.

4.2.2 Fibre response

Damage elasticity is employed to define the material response along the fibre directions. After damage initiation, the effective stresses are calculated based on the updated stress state as

$$\begin{aligned}
\bar{\sigma}_{1+} &= \frac{\sigma_{11}}{1-d_{1+}} \\
\bar{\sigma}_{1-} &= \frac{-\sigma_{11}}{1-d_{1-}} \\
\bar{\sigma}_{2+} &= \frac{\sigma_{22}}{1-d_{2+}} \\
\bar{\sigma}_{2-} &= \frac{-\sigma_{22}}{1-d_{2-}}
\end{aligned} \tag{2}$$

where d_{1+} , d_{1-} , d_{2+} and d_{2-} are the tensile and compressive damage along the fibre in the ply directions 1 and 2, respectively.

It is noted that the effective stresses are directly related to the thermodynamic forces (damage energy release rates), Y_i , that are work conjugate to the damage variables, through the relationship $\bar{\sigma}_i = \sqrt{2E_i Y_i}$. Therefore, the fibre damage variables depend only on the corresponding thermodynamic force [31].

During the analysis, the damage activation functions, F_i , are used to define the elastic domain

$$\begin{aligned}
F_i &= \phi_i - r_i \leq 0 \\
\phi_i &= \frac{\bar{\sigma}_i}{X_i}; (i = 1+, 1-, 2+, 2-)
\end{aligned} \tag{3}$$

where X_i are the tensile (+) and compressive (–) strength for uniaxial loading along the fibre directions 1 and 2. The damage thresholds (r_i) are initially set to one. After damage activation ($\phi_i = 1$), the damage thresholds at any given time (t) increase based on

$$r_i(t) = \max \phi_i(t^*); t^* \leq t \tag{4}$$

Hence, the model assumes that the ply material is non-healing. Therefore, on unloading, after damage, the damage parameters remain constant until a higher damaging load is re-applied. The evolution of damage variables are a function of the damage thresholds (r_i), the elastic energy density per unit volume at the point of damage initiation (g_0^i), the fracture energy per unit area under uniaxial tensile/compressive loading (G_f^i), and the characteristic length of the FE mesh (L_c). The damage variables are formulated as

$$d_i = 1 - \frac{1}{r_i} e^{\left(-\frac{2g_0^i L_c}{G_f^i - g_0^i L_c} (r_i - 1) \right)} \tag{5}$$

where L_c is the square root of the area (\sqrt{A}) of the largest element in the model. The elastic energy density per unit volume at the point of damage initiation is given as

$$g_0^i = \frac{X_i^2}{2E_i} \quad (6)$$

Besides, $G_f^i \approx L_{\max} E_f^i$ where L_{\max} is the maximum element length (4.5 mm in this study) to avoid over prediction of energy dissipation. E_f^i is the input energy per unit volume of the uniaxial tensile/compressive coupons up to the point of failure and is defined as

$$E_f^i = \frac{0.5 \times \sigma_f^i \times \delta_f^i}{L} \quad (7)$$

where σ_f^i , δ_f^i and L are stress at failure, displacement at failure and length of test coupons, respectively. For detailed characterisation of material behaviour, the reader is referred to [1].

4.2.3 Shear response

The shear behaviour and the mechanism of ply in-plane shear degradation are mainly controlled by the resin [34]. As such, fibre and shear damage modes are decoupled. Whilst the material response along the fibre direction remains elastic, the shear response is dominated by the nonlinear behaviour of the matrix, which may be inelastic and/or irreversible due to the presence of extensive matrix cracking or plasticity. On unloading, this can lead to permanent deformations (plastic strains) in the ply. In evaluating the shear response of the woven composite of the study, matrix elasticity, plasticity and evolution of damage are consequently modelled which are described hereafter.

4.2.3.1 Elasticity

The elastic response of the matrix relates the effective stress to the elastic strain, as follows

$$\bar{\sigma}_{12} = \frac{\sigma_{12}}{1-d_{12}} = 2G_{12}\varepsilon_{12}^{el} = 2G_{12}(\varepsilon_{12} - \varepsilon_{12}^{pl}) \quad (8)$$

where ε_{12} , ε_{12}^{el} and ε_{12}^{pl} are total, elastic and plastic strains, respectively. It should be mentioned that plasticity is only associated with the matrix and therefore, fibre plasticity is zero, i.e. $\varepsilon_{11}^{pl} = \varepsilon_{22}^{pl} = 0$.

4.2.3.2 Plasticity

An elastic domain function, otherwise known as a yield function, is introduced (F) that assumes only the effective shear stresses lead to plastic deformation, thus

$$F = |\overline{\sigma}_{12}| - R(\varepsilon^{pl}) \quad (9)$$

where $R(\varepsilon^{pl})$ is expressed in the form of a Ramberg-Osgood hardening curve, as

$$R(\varepsilon^{pl}) = \overline{\sigma}_{y0} + C(\varepsilon^{pl})^p \quad (10)$$

in which $\overline{\sigma}_{y0}$ is the initial effective shear yield stress and C and p are material parameters which are obtained experimentally [1]. It should be noted that the condition of $F < 0$ corresponds to stress states inside the elastic domain where the material endures elastic damage. On the other hand, $F = 0$ describes the plastic deformations. $F > 0$ means that the effective shear stress value is above the yield stress which is not allowed. The evolution of the plastic work during yielding (\dot{U}^{pl}) is given as a function of the evolution of the plastic strain (ε_{12}^{pl}), the shear damage parameter (d_{12}) and the effective shear stresses ($\overline{\sigma}_{12}$), as

$$\dot{U}^{pl} = 2\sigma_{12}\varepsilon_{12}^{pl} = 2(1 - d_{12})\overline{\sigma}_{12}\varepsilon_{12}^{pl} \quad (11)$$

4.2.3.3 Damage

It is understood that material cannot heal itself after damage has occurred. Therefore, after unloading, the damage cannot be reversed. The state of damage remains unchanged within a domain, defined by the damage activation function (F_{12}) as

$$\begin{aligned} F_{12} &= \phi_{12} - r_{12} \leq 0 \\ \phi_{12} &= \frac{\overline{\sigma}_{12}}{S} \end{aligned} \quad (12)$$

The function ϕ_{12} is the criteria for initiation of shear damage of the matrix and S is the shear strength of the ply. Since damage is a non-decreasing value, it must be monotonically increasing when damage takes place. The damage thresholds (r_{12}) are not independent variables, as they relate to the damage variable and are initially set to one. After damage activation ($\phi_i = 1$), the damage thresholds at any given time (t) increase based on

$$r_{12}(t) = \max\phi_{12}(t^*); t^* \leq t \quad (13)$$

It is assumed that the shear damage variable increases as a logarithm of r_{12} until a maximum value of d_{12}^{\max} is reached. Thus

$$d_{12} = \min(\alpha_{12}\text{Ln}(r_{12}), d_{12}^{\max}) \quad (14)$$

where α_{12} is a constant and $\alpha_{12} > 0$. d_{12}^{\max} is the maximum shear damage and $d_{12}^{\max} \leq 1$. Both α_{12} and d_{12}^{\max} are calibrated from the experimental data. [See \[1\] for detailed procedures of obtaining these parameters.](#)

4.3 Buckling and post-buckling analysis

To predict buckling, post-buckling behaviour and unstable collapse, linear eigenvalue buckling, and nonlinear explicit analysis are employed. At first, an eigenvalue buckling analysis was carried out. The subspace method was used to extract the eigenvalues of the composite laminates. For the post-buckling prediction, geometric imperfections were introduced to the model to trigger the unstable response within the explicit analysis. An initial qualitative comparison of the experimental buckling mode shapes and the numerical eigenvalue mode shapes was undertaken (for both laminate types 1 and 2) to select the imperfections to be modelled. This was followed by a sensitivity study to select the imperfection magnitude.

Figure 4a and Figure 5a show that experimental out of plane deflections of both type 1 and type 2 laminates are symmetric about the centre line of the specimen, and similar to the first numerical eigenvalue mode of the laminate (see Figure 4b and Figure 5b). Therefore, 10% of the laminate thickness times eigenvalue mode 1 was chosen as the initial geometric imperfection (for both type 1 and 2 laminates) after a series of imperfection sensitivity studies in which the minimum magnitude was identified which would produce the desired experimental mode shape.

In addition to the initial imperfections, the material failure law, as defined in section 4.2, is used within each post-buckling analysis. The deletion criteria of the elements is based on exceedance of damage parameters from their critical value at all integration points through the thickness (24 and 30 integration points through the thickness for type 1 and 2, respectively) for either of the fibre or matrix damage modes, or when the plastic strain due to shear deformation reaches a maximum specified value (0.025 for CFRP and 0.03 for GFRP), or when the principal logarithmic strains in the fibre direction reaches a maximum specified value (0.014 for CFRP and 0.028 for GFRP).

It is worth noting that the critical damage parameters for d_1 , d_2 , d_{12} for CFRP and d_{12} for GFRP are 1, 1, 0.67 and 0.72, respectively. It should be noted that the abovementioned strains and damage parameters come from an extensive study carried out by the authors on the material characterisation of AX-3180 and AX-5180 as reported in [1]. For accuracy and efficiency, a quasi-static analysis was performed by applying the imposed displacement using the ABAQUS/Explicit built-in load amplitude function called SMOOTH STEP. This uses a fifth order polynomial function to apply the load and eliminate significant energy changes at the start and end of loading. Additionally, mass scaling (with scale factor of 50) was applied, to decrease the computational time without increasing the loading rate.

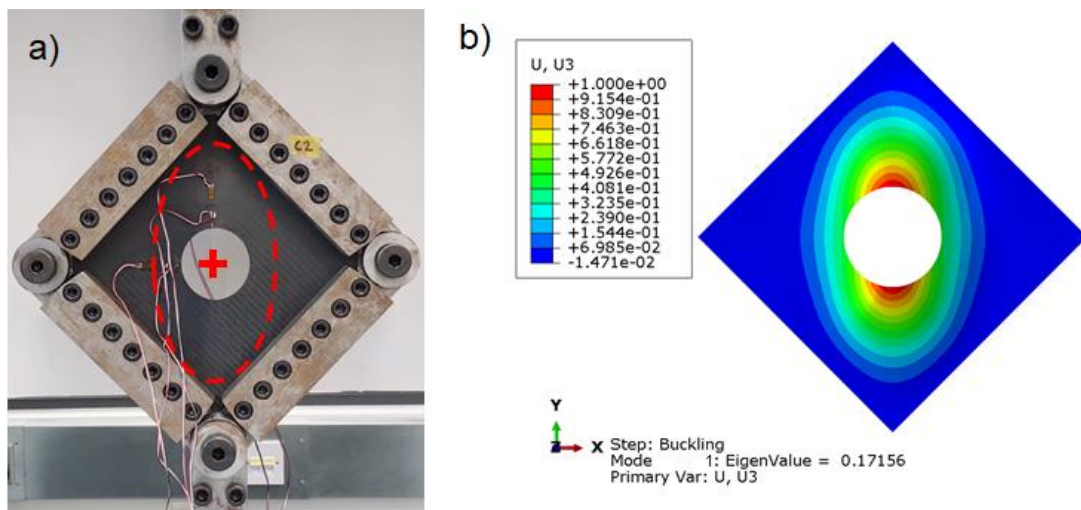


Figure 4: Qualitative comparison of experimental and numerical mode shapes for type 1 laminates; a) experimental mode shape, b) numerical first mode shape (eigenvalue of 0.172) for imposed end displacement of 2 mm equivalent to numerical buckling load of 16.55 kN

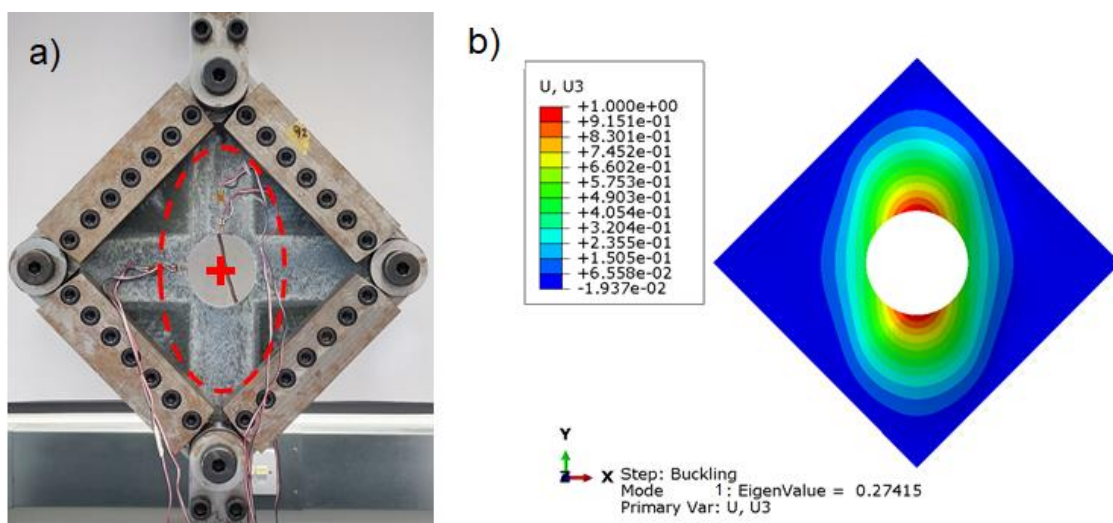


Figure 5: Qualitative comparison of experimental and numerical mode shapes for type 2 laminates; a) experimental mode shape, b) numerical first mode shape (eigenvalue of 0.274) for imposed end displacement of 2 mm equivalent to numerical buckling load of 18.38 kN

5 Materials and experimental methods

5.1 Composite material and manufacture

The materials used in this study are twill woven pre-impregnated carbon fibre (AX-5180), and a twill woven pre-impregnated glass fibre (AX-3180) with mechanical properties given in Table 1. Both carbon and glass pre-pregs consist of 54% fibre by volume (60% by weight). Three laminates for each laminate type were initially hand laid to form a plate and cured in a heated press for an hour at 120° Celsius under 100 *psi* pressure. The specimens were then abrasively cut to 200 *mm* × 200 *mm*. A 64 *mm* circular drill bit was used to create the cut-outs in all specimens of both laminate types. The circular drill bit was secured to a universal vertical milling machine and the panels were clamped onto a sacrificial material and to the platform itself. The drilling operation was performed in a controlled manner at a low speed of 130 *rpm*. Throughout the drilling process, a vacuum was used alongside the drill to capture the abrasive carbon dust.

Table 1: Mechanical properties of both woven CFRP (AX-5180) and GFRP (AX-3180) fabric plies [1], [21]

Mechanical properties	Units	AX-5180 CFRP	AX-3180 GFRP
$E_{11}=E_{22}$	MPa	67094.00	30083.00
G_{12}	MPa	4831.38	4954.60
S_t^*	MPa	595.50	437.16
S_c	MPa	393.00	306.00
S_s	MPa	87.00	62.00
Strain to failure	Strain	0.01	0.02
ν_{12} (Poisson's ratio)	N/A	0.04	0.14
t_{ply}^{**}	mm	0.224	0.288

* t, c and s subscripts denote the strength of ply in tensions, compression and shear respectively.

** cured ply thickness

5.2 Shear test

All testing was performed using a 100 *kN* capacity INSTRON tensile machine and a picture frame test fixture. The laminate specimens were first clamped into the test fixture. On each edge, the specimens were clamped via grip plates of width 10 *mm*, providing gauge dimensions of 180 *mm* × 180 *mm*. The specimens were held in position and loaded by constant static friction set initially by the clamping force of the bolts (which were set to a torque of 40 *N.m* [11]). The specimens and test fixture were located in the tensile machine, and a tensile load was applied under displacement

control at a speed of 2 mm/min to the test fixture, as shown in Figure 6. This, in turn, induced a shear deformation to the test laminate. In addition, the test device was designed to ensure that the panel was under pure shear along the loading line.

To acquire strain data, all the type 1 and type 2 laminate specimens were instrumented with six uniaxial Vishay strain-gauges (see Figure 6b) to record strains at a sample rate of 50 Hz . The locations of the strain gauges were determined based on the laminate eigenvalue simulations, with the areas of a high strain selected for gauging. Therefore, strain gauges 1 and 3 were positioned at the edges of the hole with smaller strain gauges. Two larger strain gauges 2 and 4 were positioned 30 mm away from strain gauges 1 and 3 (these gauges were used to check alignment of the specimen, picture frame fixture and universal test machine and were not used as part of the buckling or post buckling characterisation). To obtain the effect of out of plane bending, two extra small strain gauges 5 and 6 were located at the exact opposite side (back face of specimens) of strain gauges 1 and 3, respectively. Strain gauges 1, 2 and 5 measured strains in the y -direction (Figure 6), in the direction parallel to the applied tensile loading. Strain gauges 3, 4 and 6 measured strains in the x -direction, perpendicular to the applied tensile loading. Detailed positioning and spacing of each strain gauge and their numbering are given in Figure 6b.

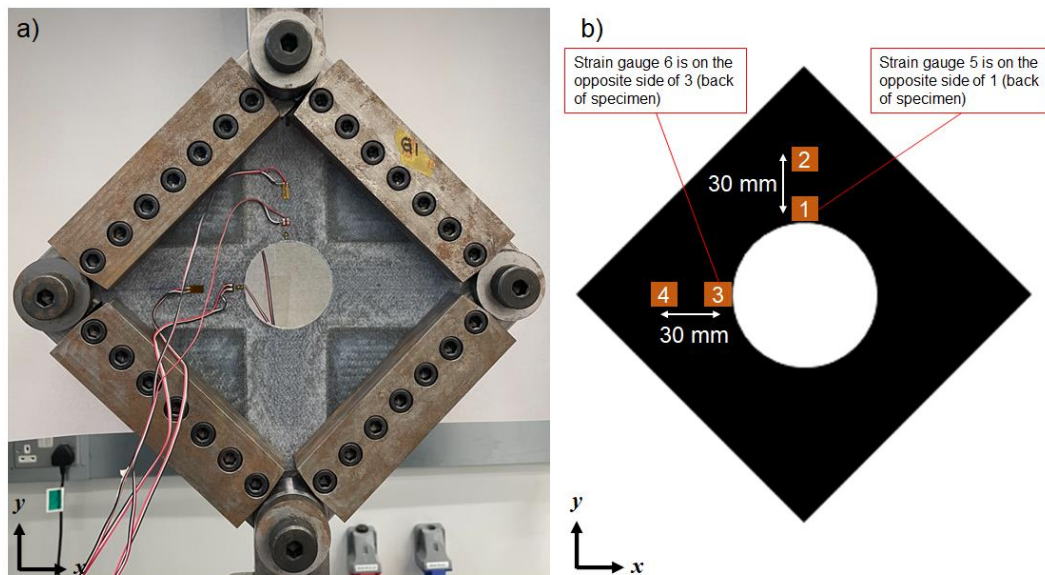


Figure 6: Shear test set-up; a) gauged laminate type 2 and b) location of strain gauges and their numbering (strain gauges 5 and 6 are on the back of the laminate opposite to strain gauges 1 and 3, respectively)

6 Buckling/post-buckling results and discussions

In this section the results obtained from the experimental and numerical studies are presented and discussed. Comparisons are made with the results obtained from the previous study [1], to shed light on the effects of creating cut-outs on overall performance of the laminates.

6.1 Load-displacement response

The experimental load-displacement curves for three type 1 and three type 2 laminates are illustrated in Figure 7. The measured load represents the tensile force applied to the test fixture, and the displacement is the resulting deflection at the loaded end of the test fixture. As expected, both laminate types, follow a linear equilibrium path up to the bifurcation point. It should be noted that there is a nonlinear response up to $\approx 0.8 \text{ mm}$ displacement for all test coupons that derives from a characteristic of the test set-up resulting from the measurement location and the settling of end fixtures and the connections to the universal test machine. After the bifurcation (red point in Figure 7), the load suddenly drops for the type 1 laminates, at $\approx 2.6 \text{ mm}$ displacement, however a reduction in the applied load does not occur for the type 2 laminates. Instead, for the type 2 laminates, the rate of load increase (slope of load-displacement curve in nonlinear region) reduces, starting from displacements $\approx 3.5 \text{ mm}$, showing a smooth transition from buckling to the post-buckling regime.

The slopes of the linear portion of each curve (between 5-20 kN) indicate specimen stiffnesses of 12.68 kN/mm and 10.37 kN/mm for type 1 and 2 laminates, respectively. Comparison with pristine specimens without cut-outs (Ref. [1]) shows that creating holes with aspect ratio of $D/L = 0.35$ leads to $\approx 38\%$ reduction in initial stiffness for the type 2 laminates.

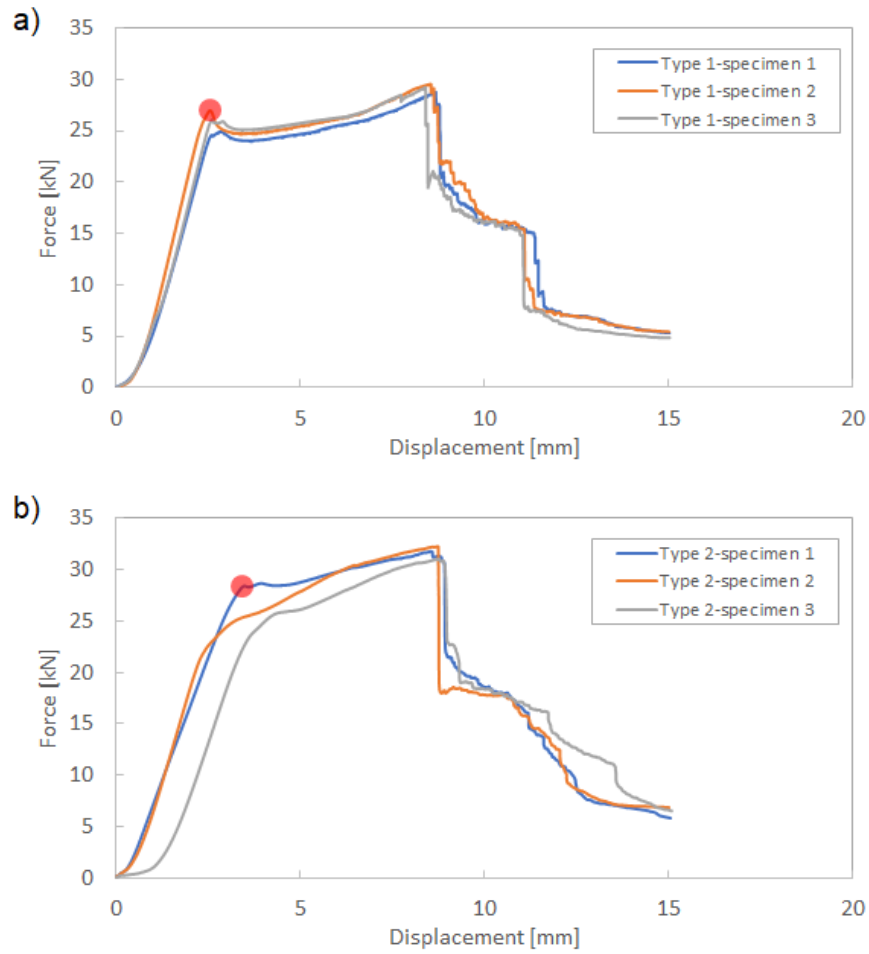


Figure 7: Buckling and post-buckling load-displacement curves for laminated composites; a) for type 1, b) for type 2 laminates of study under pure in-plane shear loading. The red point is the bifurcation load.

Table 2-3 summarises the experimental and numerical buckling and failure loads of both laminate configurations. The data in both tables show repeatable results with very low standard deviations. The average failure load of the type 2 laminates is $\approx 8.75\%$ higher than the type 1 laminates. This is despite lower experimental initial stiffness of type 2 compared to type 1 laminates. The numerical failure load is in excellent agreement with those of the experimental ones for both laminate types. Comparison with pristine specimens without cut-outs (Ref. [1]) shows that creating holes with aspect ratio of $D/L = 0.35$ leads to $\approx 28\%$ and $\approx 35\%$ reduction in failure load for type 1 and type 2 laminates, respectively. On the other hand, the experimental buckling load shows that type 1 laminates have marginally higher buckling loads than those of type 2 laminates. This is expected as the experimental stiffness of type 1 laminates are on average $\approx 18\%$ more than those of type 2. However, it should be noted that the relationship between the buckling load and stiffness of the laminates cannot be linearly correlated. For instance, 18% higher stiffness of type 1 in relation to type 2 laminates leads only to 2.58% higher buckling load for type 1 compared to type 2 laminates. Additionally, the buckling load calculated from linear eigenvalue analysis shows a considerable under-prediction of the experimental buckling load by 36% and 27% for type 1 and 2 laminates, respectively. It should be noted that in the case of pristine laminates of Ref. [1], there was an excellent agreement between the linear eigenvalue analysis and experimental buckling load. This could indicate the presence of greater imperfections or a greater sensitivity to initial imperfections, and therefore a full non-linear analysis should be used to predict buckling of structures with a large cut-out

The displacement at the moving end of the test rig at the time of specimen failure for both laminate types is approximately the same, i.e. $\approx 15\text{ mm}$, which is 3 mm less than those without cut-outs [1]. Type 2 laminates show a much greater failure to buckling load ratio. The average ratio is 1.12 for type 1 and 1.26 for type 2, demonstrating 12.5% improvement for type 2 over type 1 laminates. Unlike laminates without the cut-out (see Ref. [1]) with failure to buckling load ratio of 1.6, the existence of the cut-out has reduced the capability of the laminates to endure significant loads beyond the initial buckling. This reduction is 30% and 21% for type 1 and 2 laminates, respectively. It could be argued that type 2 laminates (X-braced hybrid design) show much less sensitivity to cut-out creation compared to type 1 design (non-hybrid). Both

laminates demonstrate behaviour similar to that of incomplete diagonal tension field panels for isotropic materials [35] in which the web of such beams retain, after buckling, some of their ability to support loads so that even near failure they are in a state of stress somewhere between that of pure diagonal tension and the pre-buckling stress. This underpins the importance of considering post-buckling behaviour for a lightweight design. For instance, in the case of aerostructure design, the structure should be designed not to buckle for the limit load, i.e. maximum load to be expected in service. However, not considering post-buckling reserve for ultimate load which is often 1.5 times the limit load, i.e. load beyond which the structure will fail, is overconservative and will lead to a heavy aerostructure design.

Table 2: Experimental and numerical force-displacement data for type 1 laminates

Type 1 Specimen ID	Experimental data					Numerical data	
	Initial stiffness (kN/mm)	Failure Load (kN)	Buckling Load (kN)	Failure/Buckling Load	Failure Displacement (mm)	Buckling Load (kN)	Failure Load (kN)
Specimen 1	13.57	28.75	26.80	1.07	15.02	16.55	28.99
Specimen 2	12.37	29.54	25.75	1.15	15.01		
Specimen 3	12.10	29.22	25.48	1.15	15.02		
Average	12.68	29.17	26.01	1.12	15.01		
Standard Deviation	0.78	0.40	0.70	0.04	0.00		

Table 3: Experimental and numerical force-displacement data for type 2 laminates

Type 2 Specimen ID	Experimental data					Numerical data	
	Initial stiffness (kN/mm)	Failure Load (kN)	Buckling Load (kN)	Failure/Buckling Load	Failure Displacement (mm)	Buckling Load (kN)	Failure Load (kN)
Specimen 1	11.83	31.81	27.94	1.14	15.05	18.38	30.10
Specimen 2	9.44	32.29	23.24	1.39	15.01		
Specimen 3	9.85	31.07	24.83	1.25	15.08		
Average	10.37	31.72	25.34	1.26	15.04		
Standard Deviation	1.28	0.61	2.39	0.13	0.04		

6.2 Experimental-numerical model validation

Before a detailed analysis and evaluation of the predicted damage mechanism using the FEM and progressive damage modelling, it is first necessary to validate the global simulation behaviour. Figure 8-Figure 9 present strain gauge data for the type 1 and 2 laminate designs, respectively. Based on Figure 8, there is good agreement between strain readings for both experimental test and numerical model for type 1, particularly up to the bifurcation points (red points). However, after the bifurcation point where extreme out of plane displacement takes place and post-buckling commences, the numerical strain readings diverge slightly. This is owing to initiation of various damage mechanisms. Similarly, based on Figure 9, the numerical strains are in good agreement with those of experiments albeit not as good as type 1. Unlike type 1, bifurcation points are not explicitly identifiable for some strain gauges, i.e. strain gauges 5 and 3. In other words, the transition from buckling to the post-buckling regime is smooth with no identifiable kink in the force-strain graph. Furthermore, unlike type 1, for type 2 laminates, the load associated to bifurcation differs for strain gauges 1 and 2. This phenomenon takes place due to initial minor local buckling around the cut-out which then changes to global buckling. Hence, smaller bifurcation load is reported for strain gauge 1 than 2. The prediction of failure load is in excellent agreement between the numerical and experimental results. It is worth noting that consideration of a perturbed geometry (instead of the ideal perfect geometry) in the numerical model significantly contributes to a smoothing of the transition between the initial linear behaviour and the nonlinear post-buckling behaviour. In addition, it also smooths the transition between modes in the post-buckling regime, thus decreasing the severity of any convergence difficulties. This is in agreement with results reported in [36], [37].

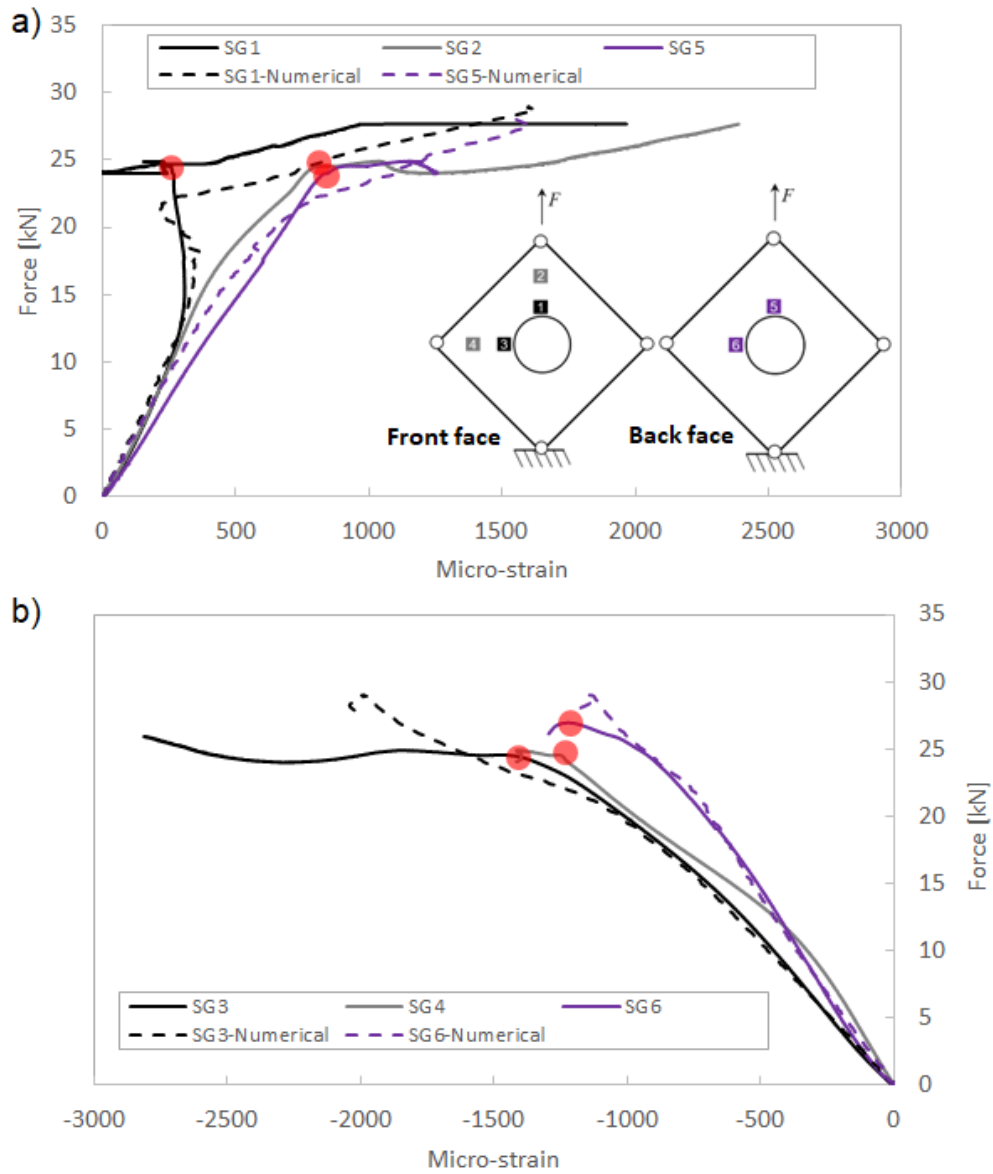


Figure 8: Experimental strain gauge readings and numerical values for pure CFRP laminates specimen 1 (type 1); a) strain readings for gauges 1, 2 and 5; b) strain gauge readings for gauges 3, 4 and 6. FEA results are extracted at through-thickness integration point locations equivalent to that of strain gauge locations in the experiment. **The red points are bifurcation points.**

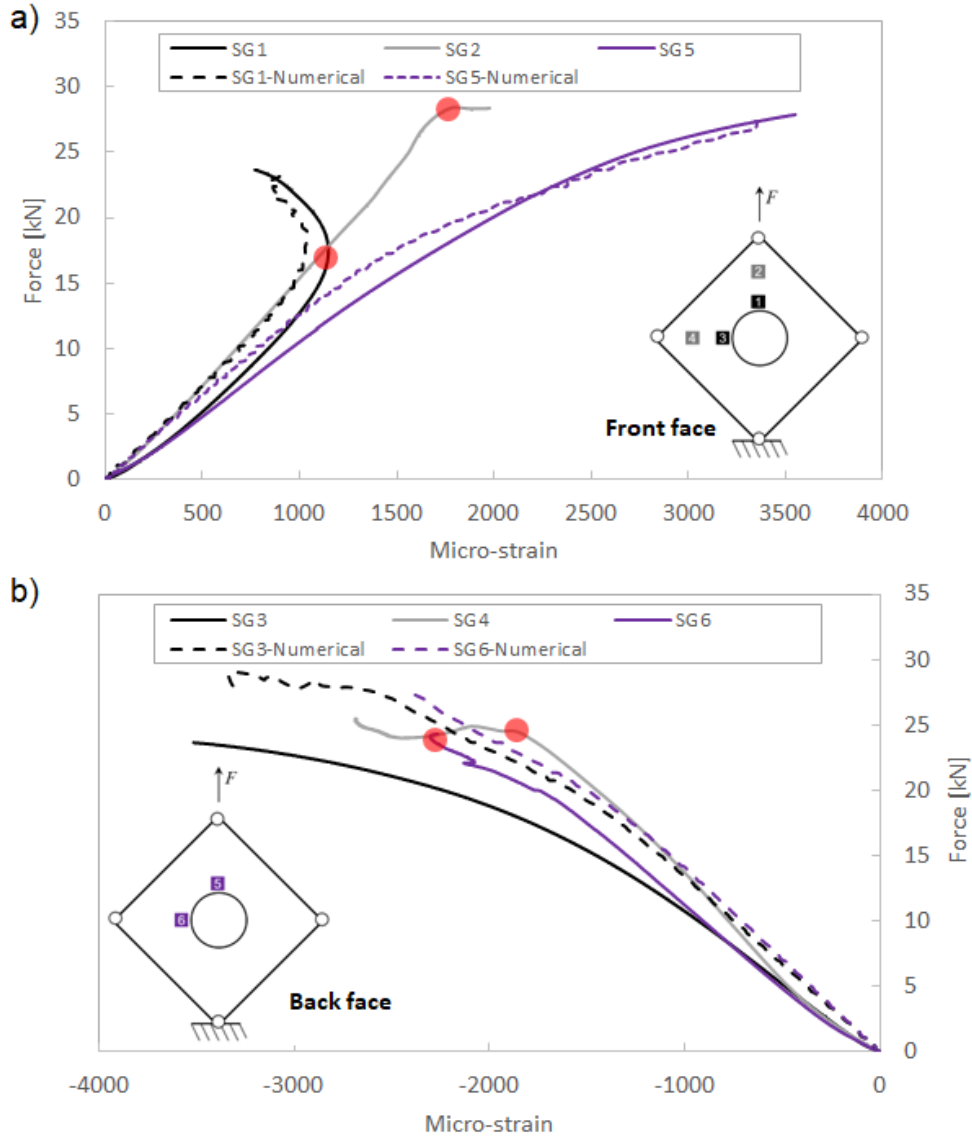


Figure 9 Experimental strain gauge readings and numerical values for hybrid CFRP-GFRP laminates specimen 3 (type 2); a) strain readings for gauges 1, 2 and 5; b) strain gauge readings for gauges 3, 4 and 6. FEA results are extracted at through-thickness integration point locations equivalent to that of strain gauge locations in the experiment. **The red points are bifurcation points.**

6.3 Damage mechanisms

In the absence of damage monitoring apparatus such as Acoustic Emission (AE) and Digital Image Correlation (DIC) to identify the initiation and propagation of various damage mechanisms including classification in the buckling and post-buckling regime [9], the numerical analysis has the advantage that it can provide insight into the internal specimen damage mechanisms, helping to identify differences in behaviour between the laminate designs. Given the good correlation between the numerical predictions and the experimental tests, as discussed in section 0, in this section, the FEA results are used to investigate various damage mechanisms.

6.3.1 Failure/collapse path

Figure 10 and Figure 11 present post-test images for all failed specimens. The figures show clear and repeatable damage shapes, damage locations, and damage path for both type 1 and 2 specimens.

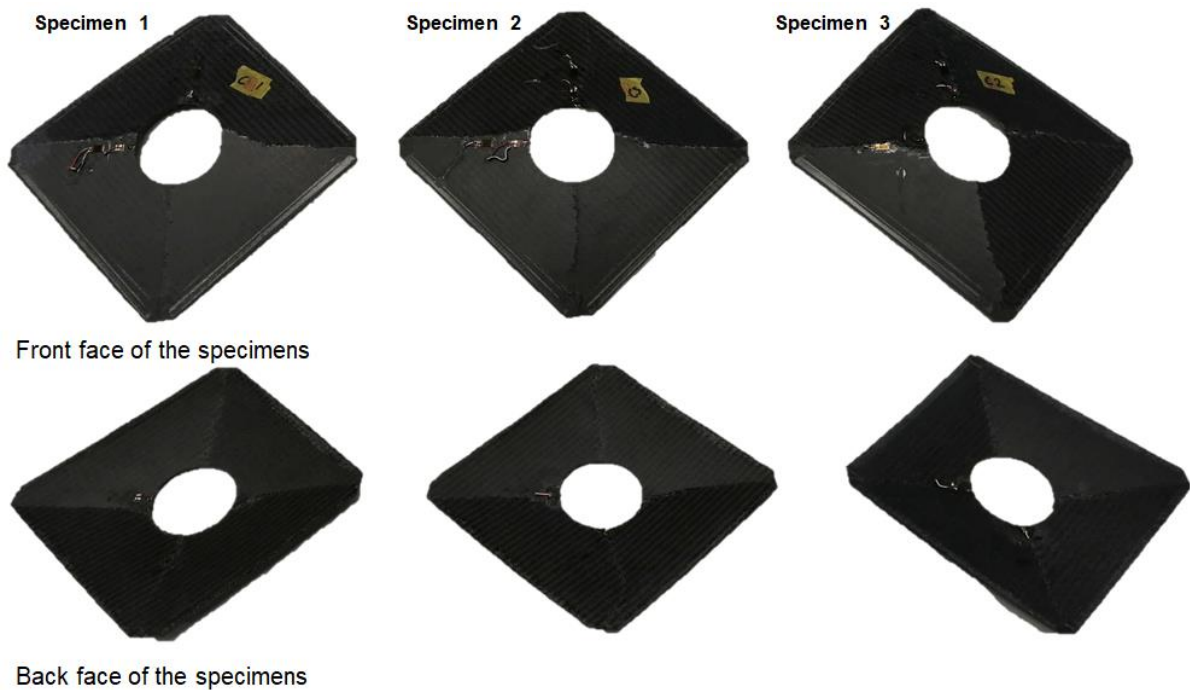


Figure 10: Front (top photos) and back (bottom photos) face of the failed specimens for type 1 laminates

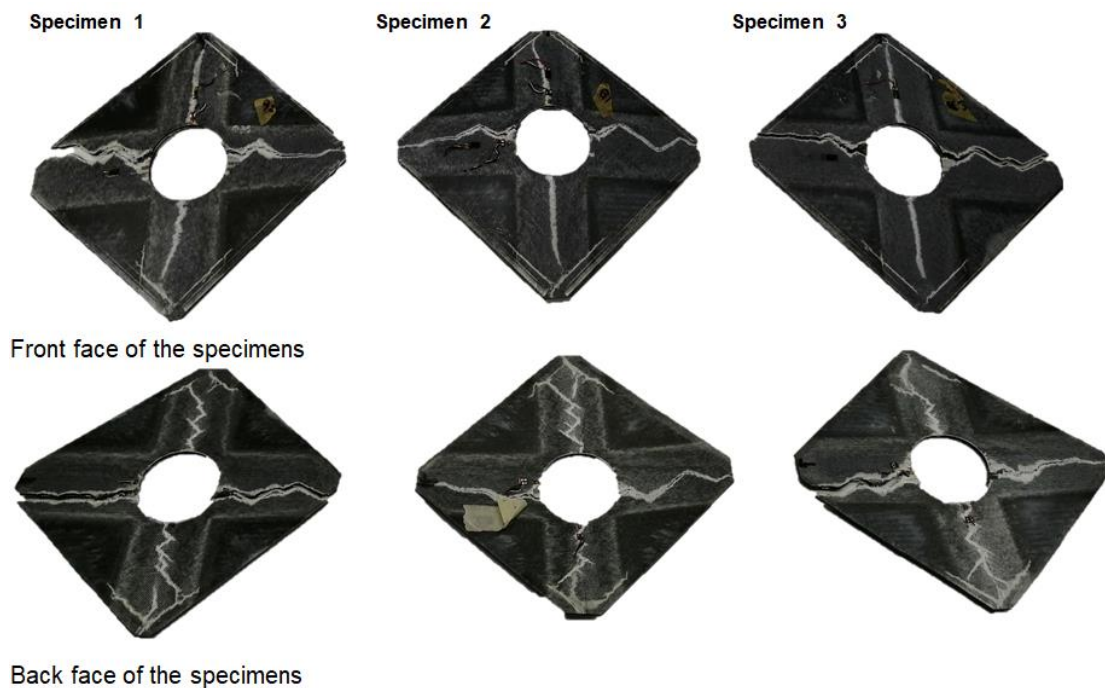


Figure 11: Front (top photos) and back (bottom photos) face of the failed specimens for type 2 laminates

Figure 12a-h illustrates the damage and failure process of the type 1 laminates. Figure 12a is at the beginning of the test, Figure 12b is at a load of $\approx 26 \text{ kN}$ when buckling takes place. After initial plate buckling, the specimen deforms into a single half-wave mode shape and continues deforming in the same mode up to the point of failure. Based on Figure 12c, the first damage starts at the right-hand edge of the cut-out. As load increases, the damage progresses on the right-hand side and simultaneously a new damage zone is formed on the left-hand edge of the cut-out (see Figure 12d). Figure 12e-f show that the damage from both edges of the cut-out continue to progress to the edge of the laminate to create a full damage line in the x direction. Concurrently, new damage lines on the outer surface of the laminate (front face) on the diagonal in the y direction appear. With further increments of displacement of the loaded end (Figure 12g-h), carbon fibres start breaking. This is accompanied by some fibre breakage or damage on the back of the specimen along the y direction. Finally, rupture of the laminate along the x direction occurs. However, no rupture is seen along the y direction. As observed in the experiment, the fracture is sudden and brittle. It is worth noting that the failure path in this study is different from findings of [9]. Kolanu et al. [9] reported failure of their laminates in the x direction but for end shortening of the loaded end (negative shear) as opposed to end extending (positive shear) used in this study. Additionally, the two studies have different laminate stacking sequences, where Kolanu et al. used uni-directional plies and a stacking sequence of $[45/90/-45/0]_S$. This suggests damage may be influenced by shear loading direction and laminate stacking sequence. Finally, examining the numerical results (Figure 13) with maximum principal strain contour plots and failed elements deleted – the agreement between modelling and test can be seen. Where both the point of initiation of the failure process (right hand edge of the cut-out) and progression of failure along the x and y directions are in excellent agreement with the experiments, Figure 12.

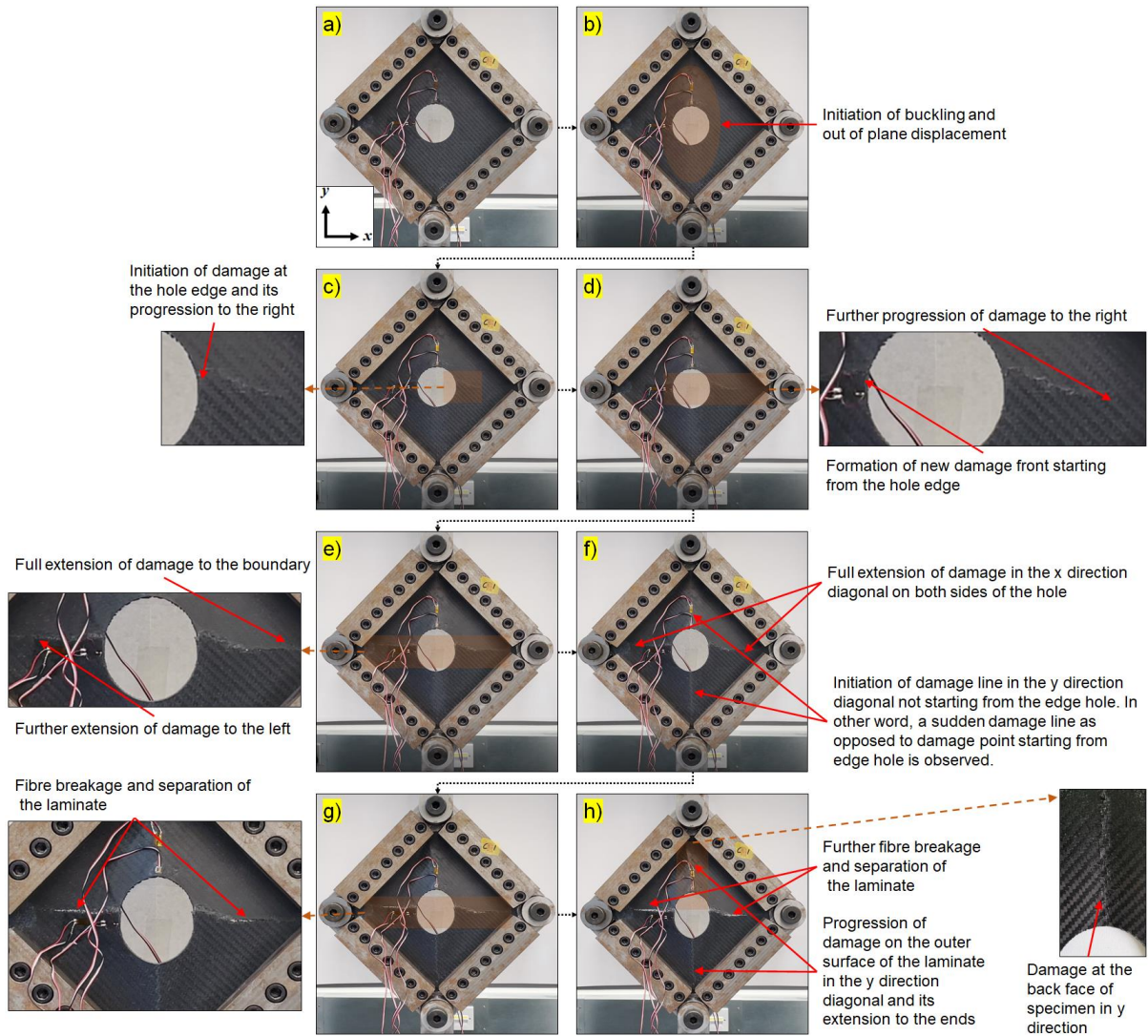


Figure 12: Experimental progression of damage and failure process in type 1 laminate

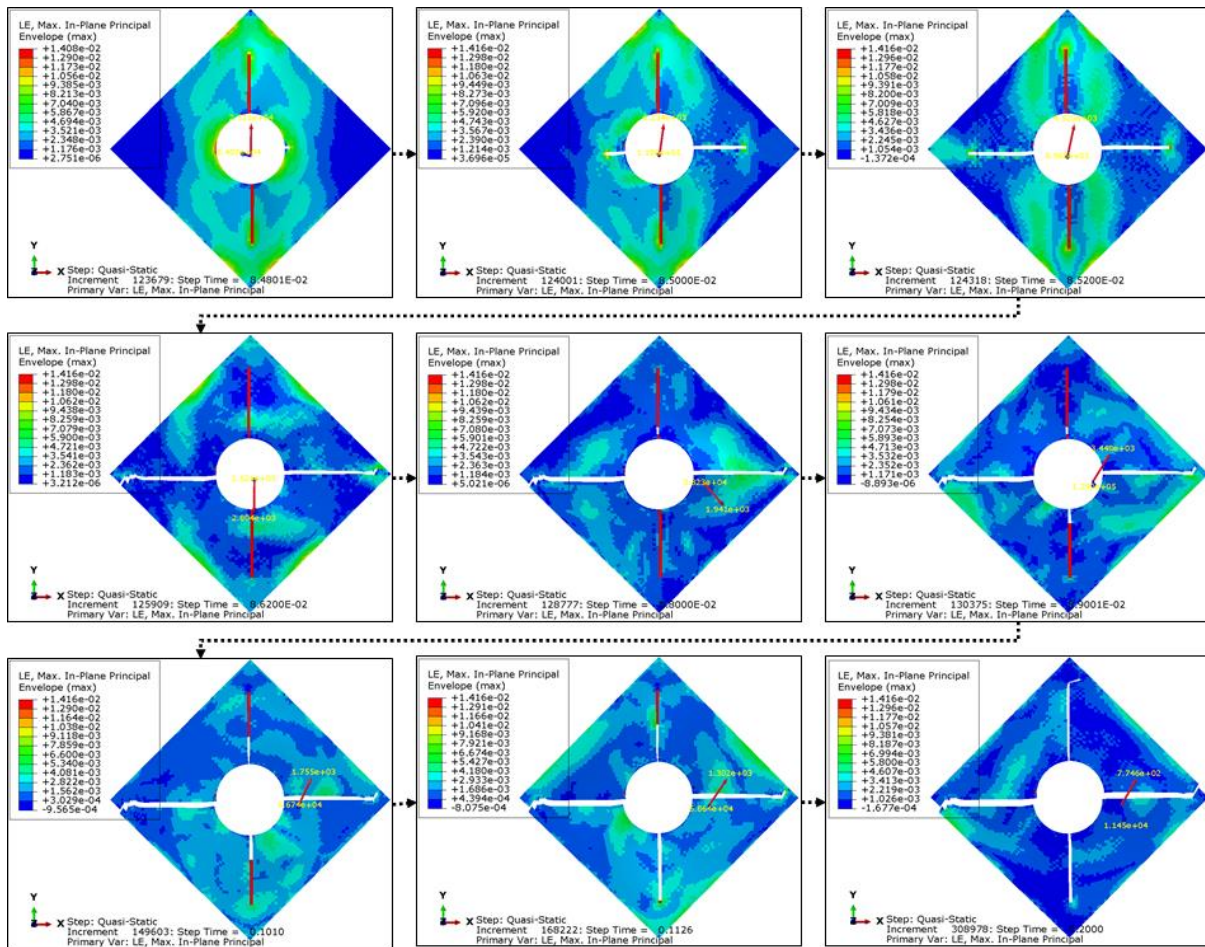


Figure 13: Failure of type 1 laminate after location 4 shown on contour plots of envelop of in-plane principal logarithmic strain (LE)

Figure 14a-h shows the progression of damage and failure of the type 2 laminate. Figure 14a is at the beginning of the test, Figure 14b is at a load of $\approx 25 \text{ kN}$, when buckling occurs. Similar to the type 1 laminate, after initial plate buckling, the specimen deforms into a single half-wave mode and continues to deform in the same mode up to the point of failure. Based on Figure 14c, the first damage starts at both edges of the cut-out. Unlike the type 1 laminates, the line connecting the centre of the cut-out to the starting point of the damage does not make a right angle with the loading direction. In fact, it makes an angle of $\approx 60^\circ$ with the loading direction based on both the experimental and numerical results. As load increases, the damage progresses to the right and left sides simultaneously in a zigzag pattern (Figure 14d-e). Thus, the damage follows a more irregular path compared to the type 1 laminate. Based on Figure 14f, as damage along the x direction reaches the edge of the laminate, full fibre breakage takes place. Then, two new damage fronts at the edge of the cut-out in the

loading direction (y direction) are formed. These damage zones then extend to the far ends of the specimen towards the loaded and fixed ends (Figure 14g-h).

Figure 15 shows the predicted maximum principal strain contour plus deleted elements. Based on the figure, similar to type 1, both the point of initiation of the failure process and progression of failure along the x and y directions are in excellent agreement with the experiments.

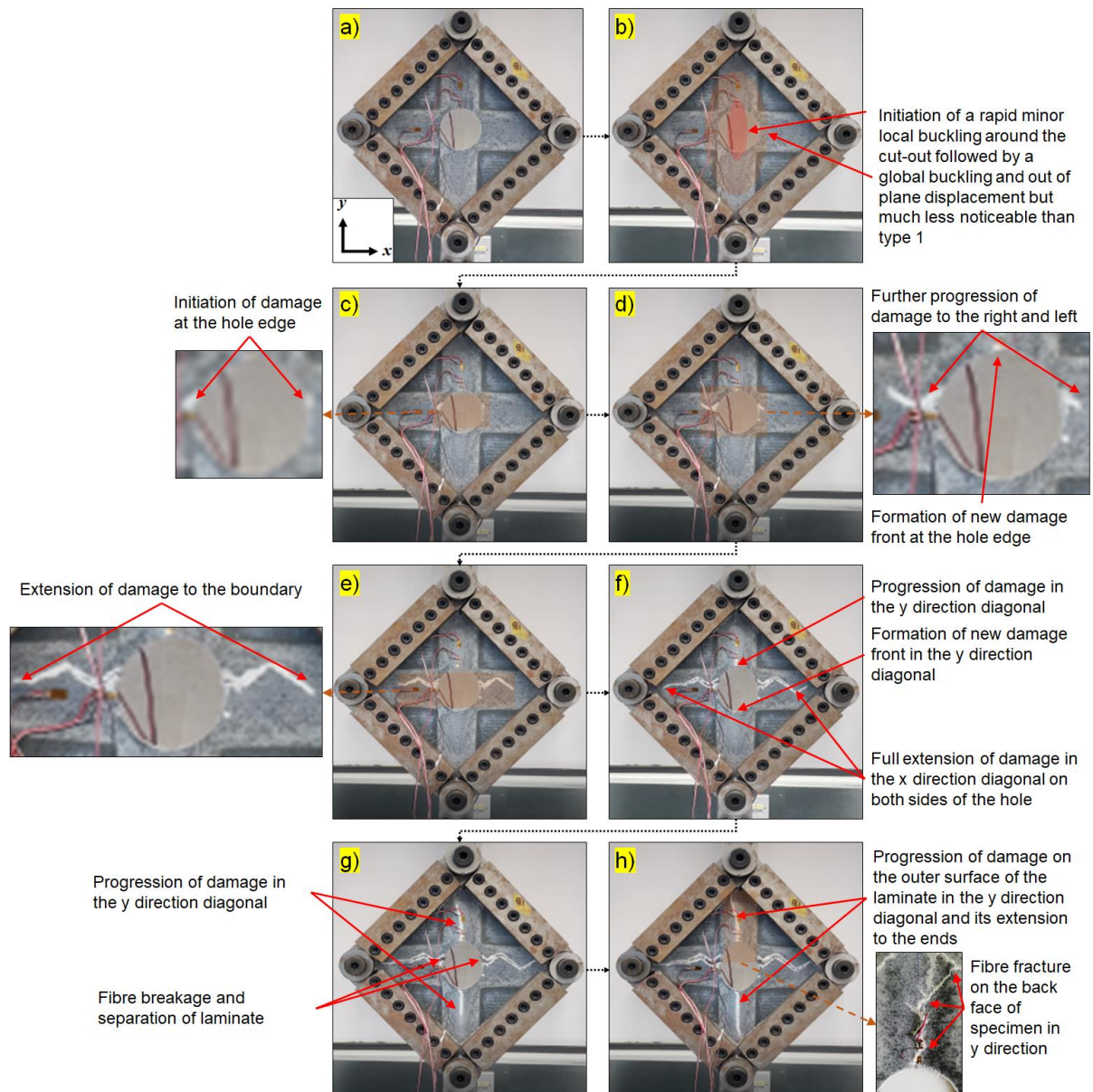


Figure 14: Experimental progression of damage and failure process in type 2 laminates

It is worth mentioning that the zigzag pattern of failure as evidenced in the experiment cannot be captured in the numerical model. To the authors knowledge this could be attributed to several factors. Firstly, the numerical model assumes

deterministic values for ply orientations. However, throughout the manufacturing process achieving exact ply orientations may not be achieved necessitating the need for the use of non-destructive quality assurance methods such as artificial intelligence-based machine vision techniques as shown in [2]. Secondly, the initial geometric imperfections used in this study and many other similar studies in the literature use extraction of natural modes via linear eigenvalue analysis. Whilst such techniques are valid and have proven to be reliable the actual measurement of plate imperfections and displacements as they take place in the experiment would provide more accurate and representative results. The reader is referred to the work of Blazquez et al. [38] for demonstration of such measurement techniques.

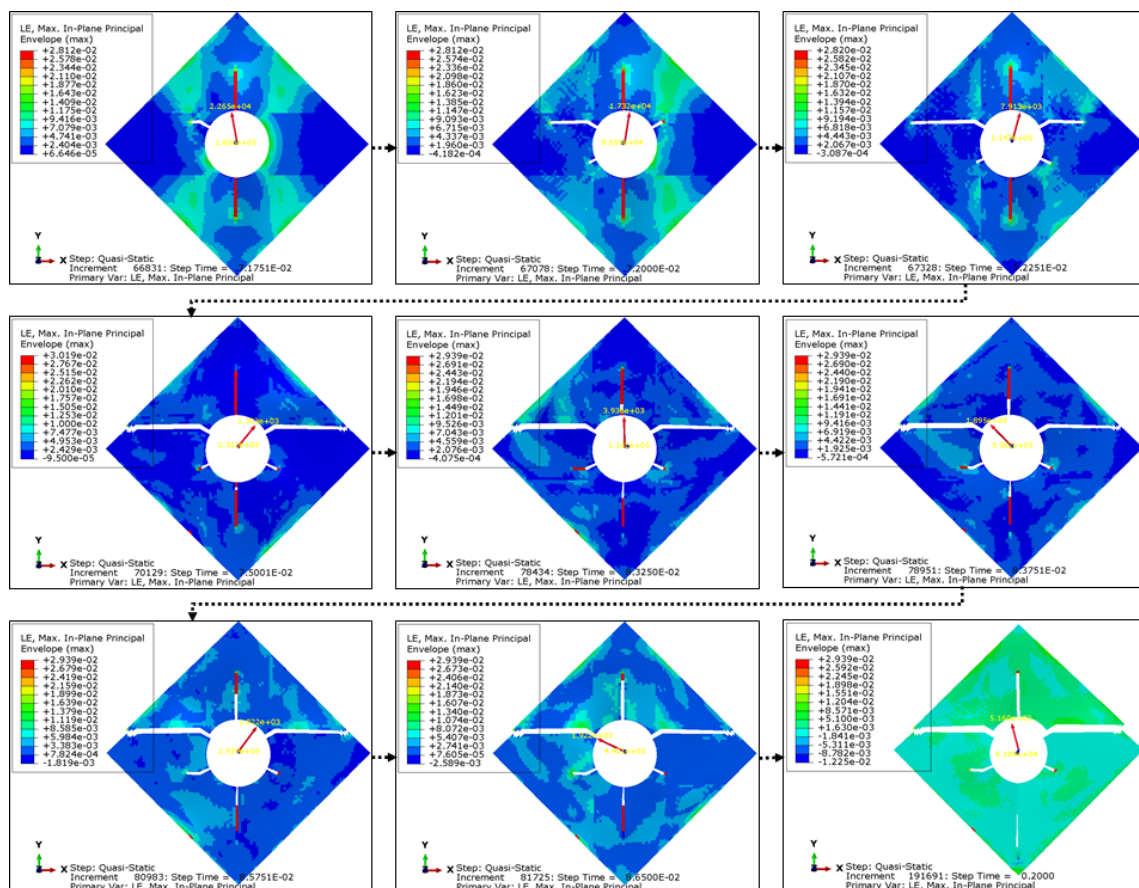


Figure 15: Failure of type 2 laminate after location 4 shown on contour plots of envelop of in-plane principal logarithmic strain (LE)

6.3.2 Damage type assessment

Figure 16 shows the envelope of damage parameters for the tensile damage along fibre direction 1 ($SDV1$), compressive damage along fibre direction 1 ($SDV2$), tensile damage along fibre direction 2 ($SDV3$), compressive damage along fibre direction 2 ($SDV4$) and shear damage ($SDV5$) at two locations (1 and 2) on the force-

displacement path of the type 1 laminates. Location 1 (Figure 16a) is associated to the numerical force of $\approx 26 \text{ kN}$ where the experimental buckling takes place. It is evident from the figure that this stage is attributed to compressive fibre damage in direction 2 (*SDV4*) particularly of ply-1 and shear damage (*SDV5*) at the edge of the cut-out. Shear damage takes place where fibre compressive damage is formed. As load drops to $\approx 24 \text{ kN}$ (Figure 16b) and at location 2, tensile damage of the fibres (*SDV3*) in the loading direction start to occur for ply-8 (front face of the laminate with orientation $\pm 45^\circ$). This is in addition to the existing shear damage and compressive fibre damage.

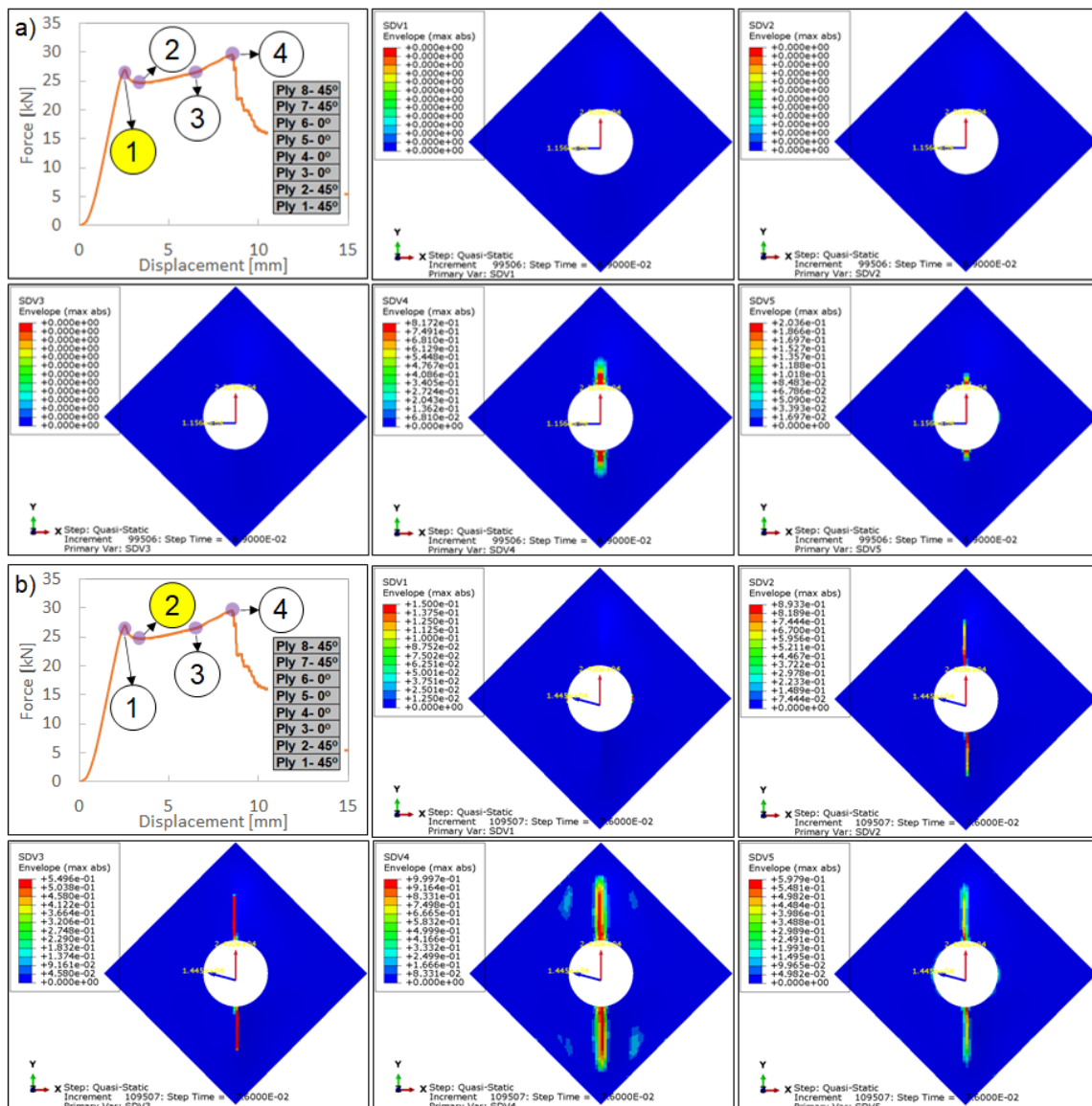


Figure 16: Envelope of damage parameters for tensile damage along fibre direction 1 (*SDV1*), compressive damage along fibre direction 1 (*SDV2*), tensile damage along fibre direction 2 (*SDV3*), compressive damage along fibre direction 2 (*SDV4*), shear damage (*SDV5*) at; a) location 1 and b) location 2 on force-displacement path of type 1 laminates (section forces and moments are illustrated as red and blue arrows, respectively)

Figure 17a, shows the damage at location 3 along the force-displacement path, where the noted damage zones have progressed with increased damage parameters. For instance, shear damage ($SDV5$) is 0.59, 0.63 and 0.64 for locations 2, 3 and 4, respectively. However, initiation of tensile damage along fibre direction 1 ($SDV1$) particularly that of ply-1 at the edge of the cut-out is observed. As the load reaches location 4 (Figure 17b), the damage reaches to higher values and up to the point of the start of specimen failure. It should be noted that up to location 4, despite the noted damage, no failure at any location is predicted (i.e. all damage values are less than 1).

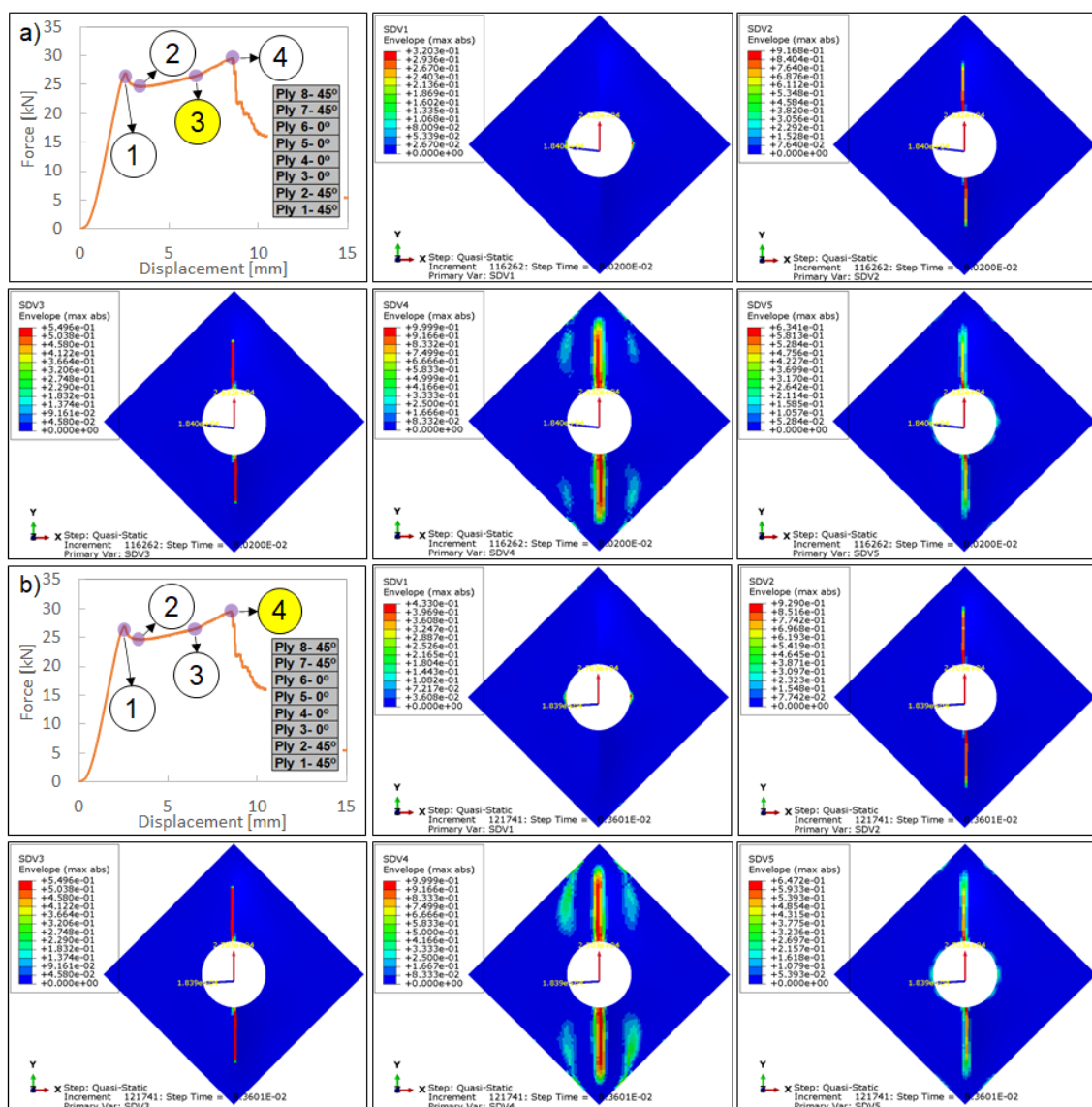


Figure 17: Envelope of damage parameters for tensile damage along fibre direction 1 ($SDV1$), compressive damage along fibre direction 1 ($SDV2$), tensile damage along fibre direction 2 ($SDV3$), compressive damage along fibre direction 2 ($SDV4$), shear damage ($SDV5$) at; a) location 3 and b) location 4 on force-displacement path of type 1 laminates

Figure 18 shows the damage parameters of the type 2 laminates at locations 1 and 2 on the experimental load-displacement response. Location 1 (Figure 18a) is associated to a load of $\approx 25 \text{ kN}$, when initial buckling occurs. At this point, compressive fibre damage (*SDV2* and *SDV4*) for all plies is observed. Furthermore, significant shear damage resulting from matrix cracking (*SDV5*) for all plies are present which distinguishes the damage type with that of type 1 at this stage. No tensile damage of fibres for any plies is noticed. As the load increases to $\approx 27 \text{ kN}$, at load-displacement point 2 (Figure 18b), the previously mentioned damage values increase commensurately. Importantly, tensile damage of fibres (*SDV1* and *SDV3*) of the GFRP ply-10 start to form. This is a similar behaviour to that of type 1 where at the same point tensile damage of fibres take place.

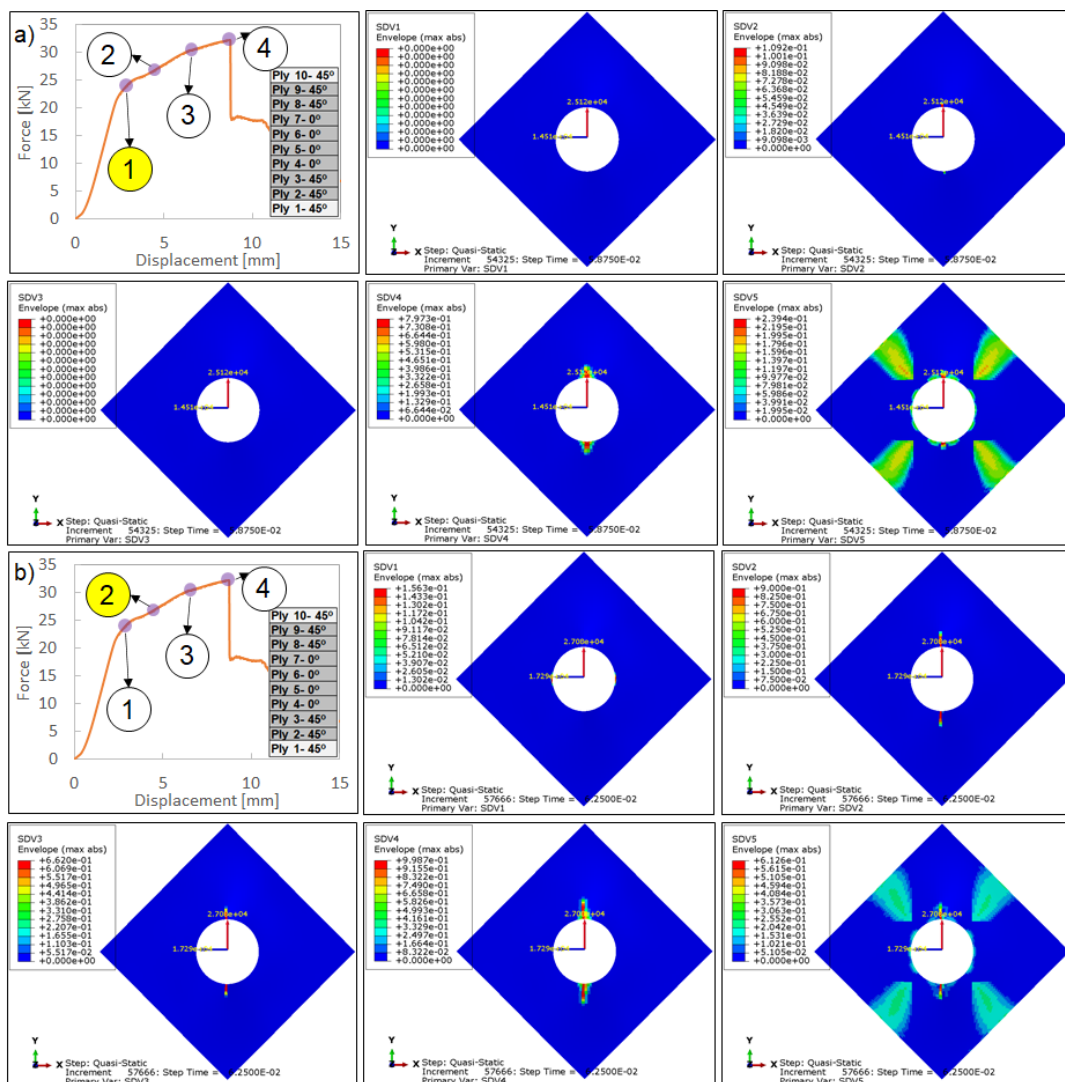


Figure 18: Envelope of damage parameters for tensile damage along fibre direction 1 (*SDV1*), compressive damage along fibre direction 1 (*SDV2*), tensile damage along fibre direction 2 (*SDV3*),

compressive damage along fibre direction 2 (*SDV4*), shear damage (*SDV5*) at; a) location 1 and b) location 2 on force-displacement path of type 2 laminates

Based on Figure 19a, point 3 represents the load of $\approx 28 \text{ kN}$. At this location the shear damage reaches its maximum permissible damage of 0.67. The compressive damage parameter of the fibres reach the value of unity for the 0° plies. Simultaneously the tensile damage of fibres increases compared to point 2. As the load progresses to the failure load of $\approx 30 \text{ kN}$ (Figure 19b), maximum fibre compressive damage and matrix shear damage takes place.

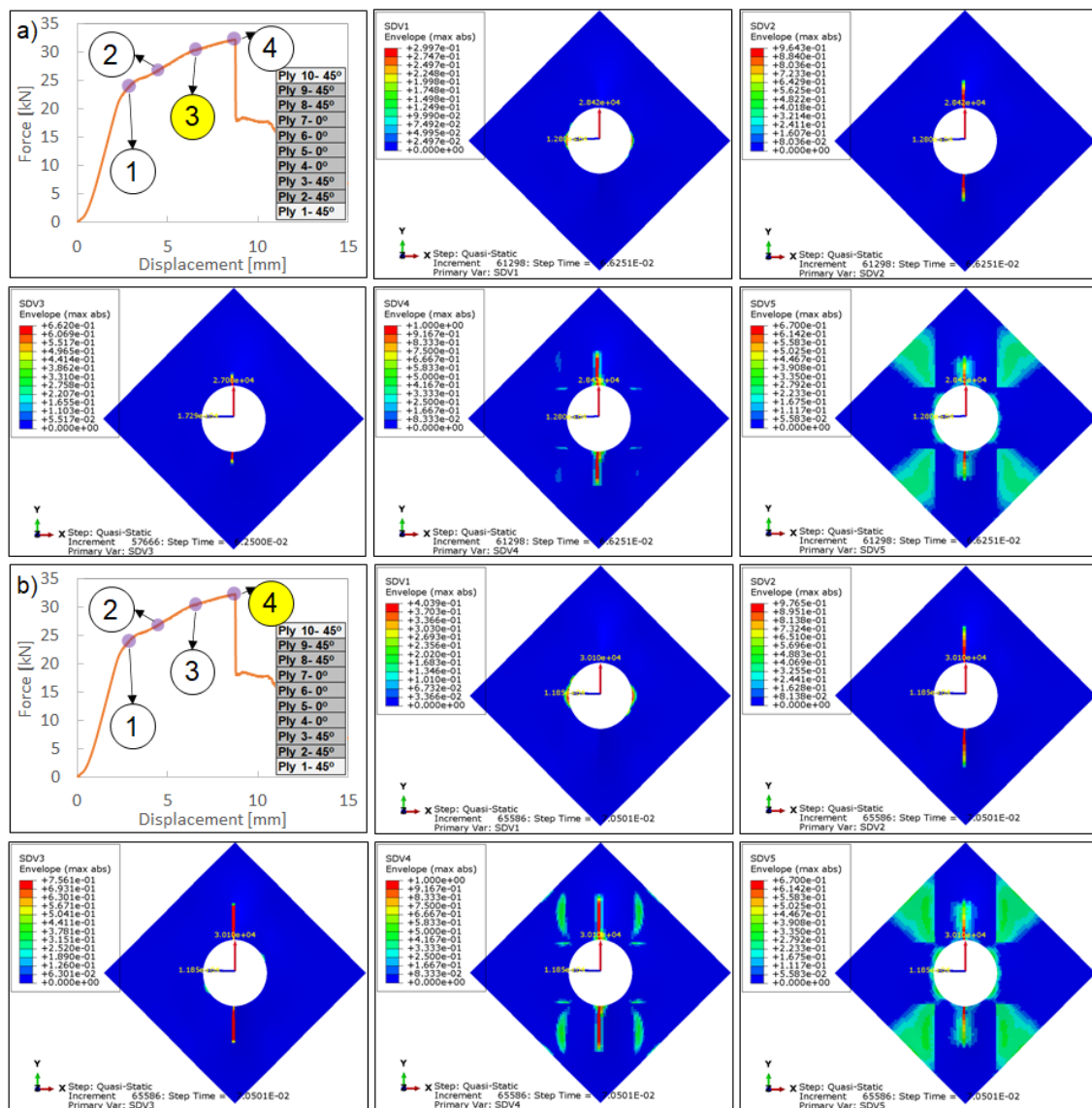


Figure 19: Envelope of damage parameters for tensile damage along fibre direction 1 (*SDV1*), compressive damage along fibre direction 1 (*SDV2*), tensile damage along fibre direction 2 (*SDV3*), compressive damage along fibre direction 2 (*SDV4*), shear damage (*SDV5*) at; a) location 3 and b) location 4 on force-displacement path of type 2 laminates

7 Conclusions

Buckling and post-buckling performance of pure twill woven CFRP (type 1) and a novel X-braced hybrid laminate design (type 2) containing a circular cut-out with $D/L = 0.35$ have been investigated experimentally and numerically, considering shear loading. The Type 1 and Type 2 laminates failed at loads approximately 1.12, 1.26 times higher, respectively, than the initial plate buckling loads, demonstrating the capability of composite laminates with cut-outs in resisting loads beyond initial buckling. However, in comparison to the failure loads of laminates without cut-outs (Ref. [1]) the cut-outs (with an aspect ratio of $D/L = 0.35$) led to significant $\approx 28\%$ and $\approx 35\%$ reduction in failure load for the type 1 and type 2 laminates, respectively. Additionally, the average failure load of the type 2 laminates was $\approx 8.75\%$ higher than type 1. The novel X-braced hybrid laminates, despite having less of the much stiffer CFRP plies, showed only marginally lower initial plate buckling performance and higher failure performance. The numerical models achieved excellent prediction of the experimental buckling and nonlinear post-buckling behaviour - predicting the bifurcation point, the failure load, the location of damage and the damage mechanisms all with reasonable accuracy. Due to the representation of initial imperfections within the numerical models, smooth transitions were consistently observed from the linear buckling to the post-buckling behaviour. Failure of the type 1 laminates initiated from the edge of the cut-out perpendicular to the loading direction whereas the initiation of failure for the type 2 laminates started from the edge of the cut-out at 60° location to the loading direction. These failures were associated to fibre tensile damage accompanied by matrix damage throughout the failure process. It should be noted that the shear damage of the matrix was considerably higher for the type 2 laminate compared to the type 1 laminate. In both laminate types, compressive damage of fibres in the loading direction then followed. The combined experimental and numerical results illustrate the feasibility to tailor the shape of hybrid laminate plies to reduce weight and maximise their post-buckling performance. Further study is required to evaluate the performance of such concepts under other loading conditions.

8 Declaration of conflicting interests

The authors declared no potential conflicts of interest with respect to the research, authorship, and/or publication of this article.

9 Acknowledgment

The authors express their gratitude to Douglas Nash and Daniel Cole (technicians at UWE) for their assistance and facilitating the research during the COVID-19 pandemic.

10 References

- [1] M. Damghani, C. Wallis, J. Bakunowicz, and A. Murphy, "Using laminate hybridisation (CFRP-GFRP) and shaped CFRP plies to increase plate post-buckling strain to failure under shear loading," *Thin-Walled Structures*, vol. 162, p. 107543, 2021, doi: <https://doi.org/10.1016/j.tws.2021.107543>.
- [2] M. Damghani *et al.*, "Design, novel quality check and experimental test of an original variable length stepped scarf repair scheme," *Composites Part B: Engineering*, vol. 230, p. 109542, Feb. 2022, doi: [10.1016/J.COMPOSITESB.2021.109542](https://doi.org/10.1016/J.COMPOSITESB.2021.109542).
- [3] C. Kassapoglou, "Applications of Advanced Composites in Aircraft Structures," in *Design and Analysis of Composite Structures*, 2nd ed., Chichester England : John Wiley & Sons Inc., 2013, pp. 1–7. doi: <https://doi.org/10.1002/9781118536933.ch1>.
- [4] A. F. Johnson, N. Toso-Pentecôte, and D. Schueler, "Numerical modelling of impact and damage tolerance in aerospace composite structures," *Numerical Modelling of Failure in Advanced Composite Materials*, pp. 479–506, Jan. 2015, doi: [10.1016/B978-0-08-100332-9.00018-9](https://doi.org/10.1016/B978-0-08-100332-9.00018-9).
- [5] V. Giurgiutiu, "Introduction," in *Structural Health Monitoring of Aerospace Composites*, Academic Press is an imprint of Elsevier, 2016, pp. 1–23. doi: [10.1016/B978-0-12-409605-9.00001-5](https://doi.org/10.1016/B978-0-12-409605-9.00001-5).
- [6] T. H. G. Megson, *Structural and stress analysis*, Third edit. Butterworth-Heinemann, 2014.
- [7] B. C. Kim, P. M. Weaver, and K. Potter, "Manufacturing characteristics of the continuous tow shearing method for manufacturing of variable angle tow composites," *Composites Part A: Applied Science and Manufacturing*, vol. 61, pp. 141–151, Jun. 2014, doi: [10.1016/J.COMPOSITESA.2014.02.019](https://doi.org/10.1016/J.COMPOSITESA.2014.02.019).

- [8] N. R. Kolanu, G. Raju, and R. M., "Post-buckling failure studies on quasi-isotropic CFRP panels under positive and negative in-plane shear loading," *Composite Structures*, vol. 246, p. 112379, 2020, doi: <https://doi.org/10.1016/j.compstruct.2020.112379>.
- [9] N. R. Kolanu, G. Raju, and M. Ramji, "Damage assessment studies in CFRP composite laminate with cut-out subjected to in-plane shear loading," *Composites Part B: Engineering*, vol. 166, pp. 257–271, 2019, doi: [10.1016/j.compositesb.2018.11.142](https://doi.org/10.1016/j.compositesb.2018.11.142).
- [10] A. W. Leissa, "Buckling of composite plates," *Composite Structures*, vol. 1, no. 1, pp. 51–66, Jan. 1983, doi: [10.1016/0263-8223\(83\)90016-8](https://doi.org/10.1016/0263-8223(83)90016-8).
- [11] A. K. Noor, "Stability of multilayered composite plates," *Fibre Science and Technology*, vol. 8, no. 2, pp. 81–89, 1975, doi: [https://doi.org/10.1016/0015-0568\(75\)90005-6](https://doi.org/10.1016/0015-0568(75)90005-6).
- [12] N. R. Kolanu, G. Raju, and M. Ramji, "A unified numerical approach for the simulation of intra and inter laminar damage evolution in stiffened CFRP panels under compression," *Composites Part B: Engineering*, vol. 190, p. 107931, Jun. 2020, doi: [10.1016/J.COMPOSITESB.2020.107931](https://doi.org/10.1016/J.COMPOSITESB.2020.107931).
- [13] A. Castriota, V. Dattoma, B. Gambino, R. Nobile, and A. Saponaro, "Experimental behavior of a CFRP damaged panel subjected to compressive stress," *Procedia Structural Integrity*, vol. 24, pp. 279–288, 2019, doi: <https://doi.org/10.1016/j.prostr.2020.02.025>.
- [14] D. Fernández, B. Begemann, P. Middendorf, and P. Horst, "Investigation of the buckling and load-bearing behaviour of selectively stitched stiffened CFRP panels under multiaxial loading," *CEAS Aeronautical Journal*, vol. 10, no. 3, pp. 703–717, 2019, doi: [10.1007/s13272-018-0343-y](https://doi.org/10.1007/s13272-018-0343-y).
- [15] Y. Feng, H. Zhang, X. Tan, T. An, Y. He, and J. Zheng, "Investigation on the buckling and postbuckling performance of aero stiffened composite panels under axial compression," *Polymer Composites*, vol. 39, no. 7, pp. 2547–2559, Jul. 2018, doi: <https://doi.org/10.1002/pc.24239>.

- [16] M. Damghani, J. Bakunowicz, and A. Murphy, "Understanding the influence of laminate stacking sequence on strain/stress concentrations in thin laminates at repair holes with large scarf angles," *Journal of Composite Materials*, vol. 53, no. 28–30, pp. 4273–4284, Jun. 2019, doi: 10.1177/0021998319855772.
- [17] M. Damghani, C. Harrison, and D. Kennedy, "The effects of composite laminate stiffness and loading on stress resultant concentration factor around a hole," *Proceedings of the Institution of Mechanical Engineers, Part C: Journal of Mechanical Engineering Science*, vol. 232, no. 6, p. 0954406218755187, Jan. 2018, doi: 10.1177/0954406218755187.
- [18] J. Zhang, W. Liu, and W. Gao, "Failure Behavior and Strength of Composite I-Section Beam with Double Cutouts and Stiffener Reinforcement," *Applied Composite Materials*, vol. 25, no. 6, pp. 1385–1400, 2018, doi: 10.1007/s10443-018-9672-6.
- [19] M. Çelebi *et al.*, "Bending of Composite Cylindrical Shells with Circular Cutouts: Buckling and Failure Analysis," *Journal of Aircraft*, vol. 56, no. 4, pp. 1551–1564, Jul. 2019, doi: 10.2514/1.C035246.
- [20] D. M. Li, C. A. Featherston, and Z. Wu, "An element-free study of variable stiffness composite plates with cutouts for enhanced buckling and post-buckling performance," *Computer Methods in Applied Mechanics and Engineering*, vol. 371, p. 113314, 2020, doi: <https://doi.org/10.1016/j.cma.2020.113314>.
- [21] M. Damghani, N. Ersoy, M. Piorkowski, and A. Murphy, "Experimental evaluation of residual tensile strength of hybrid composite aerospace materials after low velocity impact," *Composites Part B: Engineering*, vol. 179, p. 107537, Dec. 2019, Accessed: Nov. 06, 2019. [Online]. Available: <https://www.sciencedirect.com/science/article/abs/pii/S1359836819337631>
- [22] M. Fotouhi, M. Jalalvand, and M. R. Wisnom, "Notch insensitive orientation-dispersed pseudo-ductile thin-ply carbon/glass hybrid laminates," *Composites Part A: Applied Science and Manufacturing*, vol. 110, pp. 29–44, Jul. 2018, doi: 10.1016/J.COMPOSITESA.2018.04.012.
- [23] P. Taraghi, H. Showkati, and T. Zirakian, "Buckling stability performance assessment of CFRP-strengthened conical shells under uniform external

- pressure,” *Thin-Walled Structures*, vol. 148, p. 106618, 2020, doi: <https://doi.org/10.1016/j.tws.2020.106618>.
- [24] M. Genedy, S. Daghash, E. Soliman, and M. M. R. Taha, “Improving Fatigue Performance of GFRP Composite Using Carbon Nanotubes,” *Fibers*, vol. 3, no. 1. 2015. doi: 10.3390/fib3010013.
- [25] P. Taraghi, H. Showkati, and S. E. Firouzsalar, “The performance of steel conical shells reinforced with CFRP laminates subjected to uniform external pressure,” *Construction and Building Materials*, vol. 214, pp. 484–496, 2019, doi: <https://doi.org/10.1016/j.conbuildmat.2019.04.015>.
- [26] M. Maali, B. Bayrak, M. Kiliç, M. Sagiroglu, and A. Cüneyt Aydın, “Buckling behavior of double-layered composite cylindrical shells,” *International Journal of Pressure Vessels and Piping*, vol. 191, p. 104328, 2021, doi: <https://doi.org/10.1016/j.ijpvp.2021.104328>.
- [27] S. Vummadisetti and S. B. Singh, “Buckling and postbuckling response of hybrid composite plates under uniaxial compressive loading,” *Journal of Building Engineering*, vol. 27, p. 101002, 2020, doi: <https://doi.org/10.1016/j.jobbe.2019.101002>.
- [28] X. Wu, J. D. Fuller, M. L. Longana, and M. R. Wisnom, “Reduced notch sensitivity in pseudo-ductile CFRP thin ply angle-ply laminates with central 0° plies,” *Composites Part A: Applied Science and Manufacturing*, vol. 111, pp. 62–72, 2018, doi: <https://doi.org/10.1016/j.compositesa.2018.05.011>.
- [29] J. Galos, “Thin-ply composite laminates: a review,” *Composite Structures*, vol. 236, p. 111920, 2020, doi: <https://doi.org/10.1016/j.compstruct.2020.111920>.
- [30] “ABAQUS Standard/Explicit.” Dassault Systèmes Simulia Corp, United States, 2015.
- [31] A. F. Johnson and M. Holzapfel, “Modelling soft body impact on composite structures,” *Composite Structures*, vol. 61, no. 1–2, pp. 103–113, Jul. 2003, doi: 10.1016/S0263-8223(03)00033-3.

- [32] B. Ahmad and X. Fang, "Modeling Shear Behavior of Woven Fabric Thermoplastic Composites for Crash Simulations," *Applied Composite Materials*, vol. 27, no. 6, pp. 739–765, 2020, doi: 10.1007/s10443-020-09844-0.
- [33] A. F. Johnson, "Modelling fabric reinforced composites under impact loads," *Composites - Part A: Applied Science and Manufacturing*, vol. 32, no. 9, pp. 1197–1206, 2001, doi: 10.1016/S1359-835X(00)00186-X.
- [34] T. Lisle, C. Bouvet, M. L. Pastor, T. Rouault, and P. Marguerès, "Damage of woven composite under tensile and shear stress using infrared thermography and micrographic cuts," *Journal of Materials Science*, vol. 50, pp. 6154–6170, 2015, doi: 10.1007/s10853-015-9173-z.
- [35] T. H. G. Megson, *Introduction to Aircraft Structural Analysis*. Boston: Butterworth-Heinemann, 2010. doi: 10.1016/B978-1-85617-932-4.00015-4.
- [36] K. A. Stevens, R. Ricci, and G. A. O. Davies, "Buckling and postbuckling of composite structures," *Composites*, vol. 3, no. 26, pp. 189–199, 1995, doi: 10.1016/0010-4361(95)91382-F.
- [37] A. Blázquez, J. Reinoso, F. París, and J. Cañas, "Postbuckling behavior of a pressurized stiffened composite panel - Part II: Numerical analysis. Effect of the geometrical imperfections," *Composite Structures*, vol. 94, pp. 1544–1554, 2012, doi: 10.1016/j.compstruct.2011.12.013.
- [38] J. Reinoso, A. Blázquez, F. París, J. Cañas, and J. C. Meléndez, "Postbuckling behaviour of a pressurized stiffened composite panel – Part I: Experimental study," *Composite Structures*, vol. 94, no. 5, pp. 1533–1543, 2012, doi: <https://doi.org/10.1016/j.compstruct.2011.12.014>.